Aalborg University

Master's thesis

Design and Fabrication of a MEMS Device to Characterize Electromechanical Coupling in Thin Films

Written by:
Alba P. Millan

Supervised by:
Kjeld Pedersen

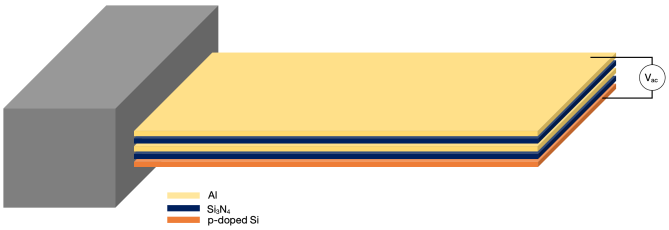

MNNF3/4
Department of Materials and Production

Fall 2022 - Spring 2023

May 31, 2023

AALBORG UNIVERSITY
DENMARK

Aalborg University
Department of Materials and Production
http://www.mp.aau.dk

Title:
Design and Fabrication of a MEMS Device to Characterize Electromechanical Coupling in Thin Films

Theme:
Master's thesis

Project period:
Fall 2022 - Spring 2023

Project group:
MNNF3/4

Participant:
Alba Pérez Millan

Supervisor:
Kjeld Pedersen

Number of pages: 47

Date of completion:
May 31, 2023

Abstract

This thesis focuses on the development of a method to fabricate free-standing beams as a characterizing tool for thin film electromechanical properties. The objective is to enhance the understanding and characterization of electromechanical coupling effects in thin films. The fabrication process involves the creation of cantilever structures using techniques such as e-beam writing and anisotropic etching. The addition of a Si_3N_4 layer is explored to characterize flexoelectricity. The results show a successful cantilever fabrication and the importance of optimizing the etching process to achieve the desired etch stop effect. Additionally, the Si_3N_4 layer addition exhibits excellent results in terms of film quality and stress levels. However, the flawed contact fabrication method used for the device presents challenges, including material overlap and leakage issues. Although the device could not be tested within the allocated timeframe, an alternative method for contact fabrication is proposed. Moreover, an experimental design is outlined, providing a promising avenue for future testing and evaluation of the device's performance.

Resumé

Micro Electro-Mechanical Systems (MEMS) have revolutionized various industries through semiconductor fabrication technologies. Silicon, chosen as the primary material for MEMS devices, offers exceptional mechanical properties, compatibility with fabrication techniques, compactness, and cost-effectiveness. This research aims to develop a versatile MEMS device based on silicon cantilevers to investigate material behavior and explore the phenomenon of flexoelectricity. The use of silicon enables precise measurements, cost-effective production, and portability for on-site testing, advancing the field of MEMS and electromechanical transduction. The fabrication process for investigating electromechanical coupling effects involved several key goals.

The first goal was to design a bottom contact using doping techniques. This contact served as a substrate for the dielectric layer and was also tested as an etch stop for microcantilever beam fabrication.

The next goal was the deposition of dielectric layers. The objective was to successfully deposit multiple layers of dielectric material while maintaining the structural integrity of the beams. It was crucial to ensure the stability of the structures for the development of a reliable device. A comprehensive study was conducted to assess the quality of silicon nitride thin films used in the device. This investigation aimed to evaluate the film's properties and suitability for the desired application. Another important goal was the design and implementation of electrical contacts. A fabrication procedure was developed to create electrical contacts at both the micro and macro scales. These contacts had to meet the device's conductivity requirements, and proper isolation between the contacts was ensured. Lastly, a testing system was designed and assembled to measure the deformation response of the cantilevers when subjected to oscillation voltage applied to the contacts. This system enabled the evaluation of the flexoelectric effect in the fabricated device. The fabrication process of the cantilever beams and the addition of the Si_3N_4 layer were accomplished successfully. The results highlighted two key findings. Firstly, the beams exhibited widening during the fabrication process, emphasizing the significance of optimizing the etching process to achieve the desired etch stop effect. Secondly, the addition of the Si_3N_4 layer yielded promising outcomes, particularly in terms of film quality and stress levels. The future prospects of this thesis highlight the identified issues with the contact fabrication method employed for the device. These

issues led to material overlap between the top and bottom contacts, resulting in a leakage problem. To ensure the successful realization of the device, a comprehensive reevaluation of the contact fabrication procedure is necessary. Although it was not possible to test the device within the allocated timeframe due to the inability to refabricate the contacts, an alternative method for contact fabrication is proposed. Additionally, an experimental design is outlined, offering a promising avenue for future testing and evaluation of the device's performance. The proposed measures in this master's thesis aim to address the challenges encountered and pave the way for further advancements in the development of the device.

Table of Contents

Preface

This report is written by Alba Pérez Millan as the master thesis of the Master's degree in Nanophysics and Nanomaterials at the Department of Materials and Production at Aalborg University. This project was written over a period of 10 months from September to June 2023, with supervision from Kjeld Pedersen. This project focuses on the fabrication of a device based on free-standing cantilevers to characterize electromechanical properties of thin films. A method will be developed to fabricate the cantilevers by using heavily boron doping as an etch stop and at the same time use this first layer as a bottom contact for the device. The structures will be produced using different techniques and characterized with SEM and conductivity measurements. A testing system will also be designed. The references use the Vancouver citation system which means that citations will be given a number corresponding to a source in the bibliography. Figures, graphs, and tables without citations were carried out by the author.

A special thanks to all people that helped carrying this project out. Thanks to Kjeld Pedersen, for his ideas and for believing me every time I said I could make something happen. A million thanks to Peter Kjær and Deyong Wang for teaching me and putting up with all my beginner mistakes. Thanks to Kim Houtved for constantly risking his life to etch (maybe too much) silicon oxide. Lastly, thanks to Leonid Gurevich for poking at the same contacts for hours.

Alba Pérez Millan

1 Introduction

1.1 Motivation

The development of Micro Electro-Mechanical Systems (MEMS) through semiconductor fabrication technologies has brought advancements to various industries. To ensure the reliability of MEMS devices, it is crucial to experimentally examine micromaterials and incorporate the findings into the design process. Additionally, MEMS technology has provided a unique opportunity to precisely evaluate the mechanical properties of nanomaterials. By using silicon as the primary material for MEMS devices, we can take advantage of its exceptional characteristics and address the need for versatile material testing tools.

Silicon, the chosen material for our MEMS device, offers distinct advantages that make it an excellent choice for material testing. Its outstanding mechanical properties, dimensional stability, and compatibility with existing fabrication techniques make it a reliable option.

One significant advantage of silicon is its ability to facilitate compact and integrated device designs. Through well-established fabrication processes, multiple functionalities can be integrated onto a single chip, reducing the device size and enhancing portability. This compactness enables convenient on-site material testing, reducing the reliance on extensive laboratory infrastructure.

Moreover, silicon's mechanical properties, such as high stiffness and low thermal expansion, make it ideal for studying the electromechanical properties of thin films. Thin films play a crucial role in MEMS devices, and accurately characterizing their behavior is essential for optimizing device performance. By utilizing a silicon-based MEMS device, researchers can obtain precise and reliable measurements of thin film properties, leading to a better understanding of their mechanical response and improved design optimization.

The compatibility of silicon with established fabrication techniques is another advantage worth noting. The mature fabrication processes for silicon enable cost-effective mass production of MEMS devices. This accessibility makes the proposed MEMS device more attainable for researchers and engineers in various settings. Additionally, the ability to produce the device in large quantities ensures reproducibility and encourages widespread adoption within the scientific community.

The development of a versatile MEMS device made of silicon offers numerous advantages for material testing. Silicon's exceptional mechanical properties, compatibility with fabrication processes, compactness, and cost-effectiveness make it an ideal choice for realizing high-performance MEMS devices. This research aims to advance the field of MEMS by providing researchers with a versatile tool to investigate material behavior, improve design optimization, and broaden access to material testing capabilities. By fabricating a MEMS device based on cantilevers, we aim to develop a device that can effectively test multiple materials and accurately measure their electromechanical properties. The use of silicon as the primary material further enhances the device's performance, allowing for precise and reliable measurements, cost-effective mass production, and portability for on-site testing. By minimizing dependence on specialized equipment and laboratory infrastructure, this research strives to provide researchers and engineers with an accessible and reproducible tool for studying the mechanical characteristics of nanomaterials and advancing the field of MEMS.

In addition to material testing, the proposed silicon-based MEMS device presents a compelling opportunity to explore flexoelectricity — an emerging electromechanical phenomenon. Flexoelectricity is a unique phenomenon that has the potential to revolutionize the field of electromechanical transduction. Unlike piezoelectricity, which is limited to only a select few materials, flexoelectricity is a universal property found in all dielectrics. This means that scientists and engineers have the opportunity to explore new materials and devices that can harness the power of flexoelectricity, particularly at small scales where large gradients can be achieved. Furthermore, flexoelectricity offers a way to overcome the limitations associated with piezoelectric materials, such as biocompatibility, toxicity, and operating temperature. This opens the door to a whole new world of possibilities in the realm of electromechanical transduction. Moreover, the use of silicon as the base material in the proposed MEMS device brings significant benefits for investigating flexoelectricity. Silicon offers excellent dimensional stability, which is crucial for accurately measuring the strain gradients required to induce flexoelectric responses. Additionally, the well-established fabrication techniques for silicon allow precise control over device geometry, ensuring reproducibility and facilitating consistent investigations into flexoelectric phenomena.

1.2 Micro-electro-mechanical systems (MEMS)

MEMS, short for micro-electro-mechanical systems, refers to devices that operate on a small scale, typically with dimensions in the micrometer range. These devices utilize electric power for actuation and detection purposes. Unlike individual components, MEMS are designed, fabricated, and function as integrated systems. Notably, a significant

characteristic of MEMS is their widespread application as sensors and actuators. Sensors can include inertia, pressure, gas, and mass sensors, while actuators encompass RF switches, force actuators, and displacement actuators.

A crucial aspect of MEMS is the prominent use of silicon as the core material. Silicon offers exceptional thermal and mechanical properties, such as low thermal expansion, high melting point, high toughness, and brittleness without plastic behavior or hysteresis. Additionally, the existing microelectronics processes can be adopted or slightly modified for MEMS fabrication, allowing easy integration of silicon-based MEMS with other electronic components. Other materials like silicon-oxide, silicon-nitride, polysilicon, gallium arsenide (GaAs), aluminum, and gold are also employed to realize MEMS structures. These materials are deposited as thin films on a silicon substrate and processed through micro-fabrication techniques, including etching and deposition. A key advantage of MEMS devices lies in their micro-fabrication technology, which enables batch fabrication, producing numerous devices simultaneously. Various micro-fabrication processes like material deposition, evaporation, and etching can be applied to multiple silicon wafers concurrently, with each wafer capable of generating hundreds of MEMS devices. However, achieving high production levels requires extensive research and optimization of each micro-fabrication step to ensure stability and reliability. [1]

1.2.1 Static behavior of a microcantilever

The derivations in this whole section have been simplified for brevity, and consequently some steps have not been included. Refer to the source material for the complete procedure [1]. Let's examine the linear equation of motion for a beam under axial loading and bending. This beam is illustrated in Figure 1.1.

Consider the bending beam depicted in Figure 1.1, with a length l, uniform density ρ, cross-sectional area A, and flexural rigidity $EI(x)$, where I represents the moment of inertia of the cross-section and E is Young's modulus. The beam experiences a tensile axial force $N(x,t)$ and a distributed force per unit length $F(x,t)$. The bending moment is denoted by M, the shear force by V, and the slope angle of the beam deflection curve with respect to the horizontal line by $\theta = \frac{\partial w}{\partial x}$.

We assume that all variables on the left side of the beam element undergo small variations when moving to the other side at a distance dx. Therefore, all variables are expanded using a Taylor series up to the first order in dx, representing this small change on the right side of the beam element.

To simplify this section, we will not present the full derivation of the equation. However, it yields:

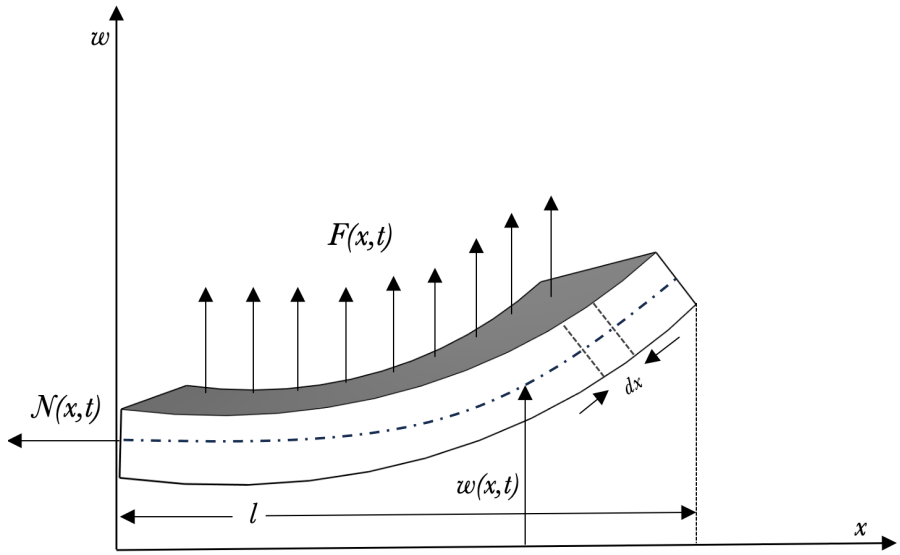

Figure 1.1: *Schematic of a clamped-free beam while bending. Inspired by [1].*

$$\frac{\partial^2}{\partial x^2}\left(EI\frac{\partial^2 w}{\partial x^2}\right) + \rho A\frac{\partial^2 w}{\partial t^2} - N\frac{\partial^2 w}{\partial x^2} = F \tag{1.1}$$

To account for distributed damping, a damping force term $Fd = -c\frac{\partial w}{\partial t}$ is added, where c is the viscous damping coefficient. The negative sign indicates that the force acts in the direction opposing the motion. Thus, the final form of the linear equation of motion becomes:

$$\frac{\partial^2}{\partial x^2}\left(EI\frac{\partial^2 w}{\partial x^2}\right) + \rho A\frac{\partial^2 w}{\partial t^2} + c\frac{\partial w}{\partial t} - N\frac{\partial^2 w}{\partial x^2} = F \tag{1.2}$$

For wide beams (with $b > 5h$) that resemble plates more than beams, Young's modulus E is replaced by $E/(1-\nu^2)$, where ν represents Poisson's ratio.

Equation 1.2 is a fourth-order partial differential equation in x, requiring four boundary conditions. These conditions can be determined based on the geometrical features of the deflection and slope, as well as the forces and moments balance at the beam ends.

Although the beam can have various boundary conditions such as simply supported (enabling rotation), free, or an edge with a rotational spring, the most common micro-cantilever configuration has a clamped support, fixing it in place. For this boundary condition, the point a refers to the left edge of the beam ($x = 0$). Consequently, this boundary condition restricts the translational and rotational motion of the beam's edge, resulting in $w(a,t) = 0$ and $\left.\frac{\partial w}{\partial x}\right|_{a,t} = 0$.

To derive the equation governing the static response of a beam, we can start with

its equation of motion and assume that the displacement is independent of time. By substituting $w = w(x)$ into Equation 1.2 and setting all the time-dependent and time derivative terms to zero, we obtain the static equation:

$$\frac{d^2}{dx^2}\left(EI\frac{d^2w}{dx^2}\right) - N\frac{d^2w}{dx^2} = F(x) \tag{1.3}$$

This equation describes the static behavior of the beam, where w represents the displacement of the beam perpendicular to the x-axis, E is the Young's modulus, I is the moment of inertia of the cross-section, N is the axial force, and $F(x)$ is the distributed force per unit length acting on the beam. The equation involves second-order derivatives of w with respect to x.

Applying the clamped-free boundary conditions of the cantilever, the analytical expression of the beam profile can be obtained as

$$w = \frac{F_0}{24EI}x^4 - \frac{F_0 l}{6EI}x^3 + \frac{F_0 l^2}{4EI}x^2. \tag{1.4}$$

From this, we know that the maximum deflection of the beam at $x = l$ is calculated as

$$w_{\max} = \frac{F_0 l^4}{8EI}. \tag{1.5}$$

Beams made of different material layers

Now, let's illustrate the procedure for a beam composed of two layers. The same approach can be applied to beams made of more than two layers.

One possible method is to use the transformed or equivalent cross-section technique. In this method, the original cross-section of the beam, consisting of different materials, is transformed into an equivalent cross-section made of a single homogeneous material. This material, denoted as material number one, has a modulus of elasticity E_1 and thickness t_1. Follow these steps:

1. Define the ratio $n = E_2/E_1$.

2. Transform the actual cross-section of the beam, comprising the two different material layers, into an equivalent cross-section with only one material. This is achieved by modifying the width of the layer made of the second material, material 2, to become nb, while keeping the width of the layer made of material 1 unchanged as b. Figure 6.5b illustrates this step.

3. Determine the centroid of the new cross-section. This defines the location of the neutral axis Y_n, where the bending stresses are zero. It can be determined using the following formula:

$$Y_n = \frac{(t_1/2 + t_2)t_1 + (t_2/2)t_2 n}{t_1 + t_2 n} \tag{1.6}$$

4. Evaluate the total or effective moment of inertia I_{eff} of the transformed cross-section around Y_n. This step involves applying the parallel axes theorem to transform the moment of inertia of each layer around its local centroid location Y_i to that around the neutral axis Y_n. For this example, we have:

$$I_{\text{eff}} = (\frac{(bt_1^3}{12} + \ t_1 b(t_2 + t_1/2 - Y_n)^2) + (\frac{nbt_2^3}{12} + \ t_2 nb(t_2/2 - Y_n)^2) \tag{1.7}$$

When modeling the behavior of this beam, use an effective flexural rigidity $E_1 I_{\text{eff}}$ in place of EI in Equation 1.2 and any associated boundary conditions involving EI. Finally, the term ρA in Equation 1.2 is calculated by summing the mass per unit length of each individual layer based on the original cross-section. In this example:

$$\rho A = b(\rho_1 t_1 + \rho_2 t_2) \tag{1.8}$$

where ρ_1 and ρ_2 are the material densities of material one and material two, respectively.

1.2.2 Microcantilever beam resonator

The mass-sensitive quartz crystal microbalance (QCM) is a widely recognized resonant sensor utilized in film deposition equipment to monitor film thickness. The deposition of additional mass on the crystal alters its resonance frequency, enabling precise measurement.

In recent years, silicon-based resonant structures have also been extensively explored for various sensor and actuator applications, complementing the quartz-based systems. These silicon structures exhibit sensitivity to not only mass changes but also other factors such as forces, torques, variations in material properties, and more. These influences impact not only the resonance frequency but also other characteristics of the structure, including vibration amplitude, quality factor, and phase. Unlike quartz, silicon is not piezoelectric, necessitating the use of multiple excitation and detection methods for these micromachined structures. [2]

One of the most prevalent types of MEMS resonators is the microcantilever. It comprises a mechanical beam anchored at one end and free to move at the other. Microcantilevers have gained significant attention in various sensing applications due to their exceptional sensitivity [3].

The resonant characteristics of microcantilevers are directly influenced by axial forces, applied torques, added mass, changes in damping, alterations in material properties, variations in the magnitude of the driving force, and modifications in the resonator's geometry. [2]

Principles

Consider a beam with dimensions: length L, width b, and thickness $h \ll b$ (where $b \ll L$) subjected to an axial force N. Refer to Figure 1.2 for the schematic diagram of the beam resonator.

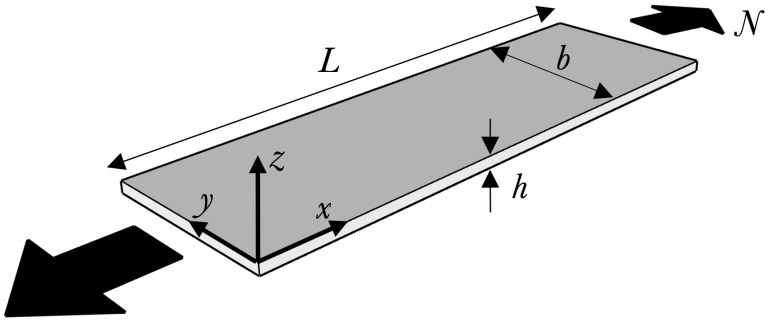

Figure 1.2: *Schematic of a beam resonator subjected to an axial load N. Inspired by [2].*

It is assumed that the transverse deflection $w(x, y, t) = w(x, t)$ varies only along the length x of the beam and that the maximum vibration amplitude $w_{\max}$ is small compared to the beam thickness. When $N = 0$, the equation of motion describing the free transverse deflection $w(x, t)$ of the beam is governed by the one-dimensional, homogeneous Euler-Bernoulli differential equation:

$$\frac{d^2}{dx^2}\left(EI\frac{d^2w}{dx^2}\right) + \rho A\frac{d^2w}{dt^2} = 0 \tag{1.9}$$

where E represents the apparent Young's modulus, I is the moment of inertia, ρ denotes the mass density, and A represents the cross-sectional area of the beam.

Neglecting the influence of air damping and additional axial forces, for typical micromachined beam structures with $b \gg h$, the apparent Young's modulus E can be calculated as:

$$E = \frac{E_1h_1 + E_2h_2}{h_1 + h_2} \tag{1.10}$$

where E_1 and E_2 represent the Young's moduli of the two different materials with thicknesses h_1 and h_2, respectively.

In the case of a uniform beam with a rectangular cross-section, the moment of inertia I can be determined as:

$$I = \frac{bh^3}{12} \tag{1.11}$$

Assuming a separation of time and space coordinates and harmonic time dependence

$w(x,t) = w(x) \cdot T(w)e^{i\omega t}$, the eigenfunctions (natural modes) and corresponding eigenvalues (natural frequencies) of Equation (1.1) can be calculated analytically. The solution of the fourth-order, homogeneous differential Equation (1.1) can be expressed as the sum of four linearly independent solutions:

$$w(x) = C_1 \cosh(\lambda x) + C_2 \sinh(\lambda x) + C_3 \cos(\lambda x) + C_4 \sin(\lambda x) \tag{1.12}$$

with constants C_1, C_2, C_3, C_4, and the dimensionless parameter λ defined as:

$$\lambda = \left(\frac{\rho A \omega^2}{EI}\right)^{1/4} \quad (1.5) \tag{1.13}$$

For a cantilever beam clamped along one edge only, the boundary conditions lead to the characteristic equation $\cos(\lambda)\cosh(\lambda) = -1$. Consequently, the coefficients λ_n used to calculate the resonance frequencies can be determined as:

$$\lambda_1 = 1.88, \quad \lambda_2 = 4.69, \quad \text{and} \quad \lambda_3 = 7.86$$

These coefficients are utilized in determining the resonance frequencies.

Excitation and detection methods

The resonant sensor comprises the resonator structure itself and various components for exciting and detecting mechanical vibrations. The fundamental components of a resonant sensor include a mechanical part, an excitation source, a detector, and feedback control circuitry. The feedback circuitry ensures the resonator maintains its desired resonance mode even when the resonance frequency changes due to variations in the measured quantity. To investigate vibrations of a resonator structure, there are six commonly used excitation techniques with their corresponding detection methods.

The first technique is electrostatic excitation and capacitive detection. It involves placing two closely spaced electrodes, where one is part of the cantilever beam, creating a parallel plate capacitor. Applying an alternating voltage to the electrodes generates an electrostatic force that deflects the cantilever beam. The same electrodes are used for detection, where the vibration of the beam alters the distance between the electrodes, resulting in a change in capacitance, which can be used to detect the vibration. This technique is particularly effective when the resonator oscillates in a vacuum to avoid air damping. The next technique is dielectric excitation and capacitive detection, which is similar to electrostatic excitation. However, a thin layer of dielectric material is sandwiched between two electrodes, with one electrode being part of the cantilever beam. The AC voltage creates an electrostatic force that laterally deforms the dielectric thin film, generating a bending moment in the beam. Vibrations cause changes in the area

between the plates, leading to a change in capacitance, which is utilized for detecting the beam's vibration.

The third method is piezoelectric excitation and detection. It utilizes a piezoelectric material like ZnO or AlN for both excitation and detection of beam vibrations. When a voltage is applied across the piezoelectric material, it undergoes physical deformation, which serves as the excitation mechanism for the resonators. The top surface of the beam is deposited with a pair of electrodes, with the piezoelectric material sandwiched in between. Applying an AC voltage to the electrodes generates stress in the piezoelectric layer, resulting in the bending of the cantilever. The reverse piezoelectric effect can be used for detecting beam vibrations. The vibrating beam causes physical deformation of the piezoelectric layer, generating an electric field across it. By measuring this electric field, the magnitude of vibration can be determined.

Resistive heating excitation and piezoresistive detection is another employed method. In this technique, excitation is achieved by exposing a selected part of the cantilever to heat pulses, causing local expansion of the material and resulting in beam deflection. The local expansion is achieved by heating up the integrated diffused resistor or polysilicon resistor. The same polysilicon resistor is used for detecting vibrations of the cantilever. Polysilicon exhibits excellent piezoresistive properties, as its resistivity changes with physical deformation. Deflection of the beam causes the integrated piezoresistor to deform physically, leading to a change in resistance. Connecting this piezoresistor to a voltage source allows for detecting the beam's vibration by monitoring the voltage drop across the piezoresistor.

The second-to-last commonly used method is optical heating excitation and optical detection. This technique involves utilizing a laser source for excitation and an optical detector for detection. The surface of the resonator is exposed to periodically activated laser beams, and the absorbed light generates the necessary thermal stress for exciting the cantilever beam. An optical arrangement is employed for vibration detection. Two primary optical detection techniques are used: interferometric detection and amplitude modulation. Interferometric detection relies on the interference fringe pattern to detect and measure the magnitude of beam displacement. Optical detection, in general, is widely used as it doesn't require additional integrated arrangements on the resonator beam.

The final technique is magnetic excitation and detection. Magnetic excitation is achieved through the Lorentz force resulting from the interaction between the surrounding magnetic field and the electric current passing through the resonating structure. Magnetic detection employs the reverse principle of magnetic excitation, where the vibrating beam (conductor) in the presence of a magnetic field generates an induced voltage. H-shaped resonators are typically utilized for this technique, with one beam responsible for excitation and the other for detection.

1.3 Electromechanical coupling as a driving force

Resonators play a crucial role in a wide range of MEMS devices, including inertial sensors, bio sensors, chemical sensors, pressure sensors, and energy harvesters. [4]

The electromechanical coupling phenomenon, which establishes a connection between electrical and mechanical properties, holds significant importance in the field of solid-state physics and practical applications. This effect is present in a wide range of materials, both natural and artificial, known as electro-active materials, capable of converting mechanical energy into electrical energy and vice versa. The technological applications of these materials are diverse, encompassing energy harvesting, where ambient energy sources like mechanical, wind, solar, or body movement are converted and stored as electrical energy, sensing, where mechanical inputs such as stress are converted into electrical outputs, and actuation, where applied electric fields generate controlled mechanical outputs, such as forces.

Piezoelectricity is a widely used and well-known electromechanical coupling effect, in which certain materials polarize in response to homogeneous stress. This effect is described mathematically as a linear relationship between stress and polarization, where d is the third-rank tensor of piezoelectricity. Additionally, piezoelectric materials also deform under an applied electrical field, as described by Equation 1.14,

$$\epsilon_{ij} = d_{ijl} E_l \tag{1.14}$$

where ϵ_{ij} is the strain tensor, d_{ijl} is the third-rank piezoelectric tensor, and E_l is the electric field. It is important to note that piezoelectric deformation reverses sign when the electric field sign is reversed, and it is scale-invariant. This effect is only possible in materials with a non-centrosymmetric atomic or molecular structure. [5–7]

Ionic crystals exhibit piezoelectric properties only in certain point groups, specifically 20 out of the 32 groups (as shown in Table 1.1). However, only a few of these groups demonstrate desirable piezoelectric characteristics. The most well-known piezoelectric materials are ferroelectric ceramics, widely used in various technologies. However, these ceramics tend to be brittle, often contain lead, and have limited operating temperature ranges [8].

Another electromechanical coupling phenomenon that has garnered significant interest in soft materials is electrostriction, also known as the Maxwell-stress effect [9]. This effect refers to the electrostatic forces generated by the Coulombic attraction between charges of opposite polarity at the electrodes, leading to deformation. Mathematically, the stress caused by electrostriction is quadratically dependent on polarization and does not change sign upon reversing the polarization (unlike piezoelectricity). While electrostriction is present in all dielectrics, its influence is typically weak and becomes significant mainly

Point Group	Centrosymmetric	Non-centrosymmetric (piezoelectric)
Triclinic	$\bar{1}$	1
Monoclinic	$2/m$	2
Orthorhombic	mmm	222, $mm2$
Tetragonal	$4/m$, $4/mmm$	4, 422, $4mm$, $\bar{4}2m$
Trigonal	$\bar{3}$, $\bar{3}m$	3, 32, $3m$
Hexagonal	$6/m$, $6/mmm$	6, 622, $6mm$, $\bar{6}m2$
Cubic	$m3$, $m3m$	23, $\bar{4}3m$, 432

Table 1.1: *Centrosymmetric and non-centrosymmetric point groups. Only the non-centrosymmetric groups are piezoelectric.*

in soft materials such as dielectric elastomers or piezoelectric polymers. Furthermore, unlike piezoelectricity, electrostriction does not exhibit a two-way coupling, as deformation does not produce an electric field. Therefore, electrostriction is not suitable for sensing applications.

The study of piezoelectricity has a long history in the field of materials mechanics, dating back to its initial discovery by Pierre and Jacques Curie in 1880.

1.3.1 Flexoelectricity

Flexoelectricity is a more recently discovered electromechanical coupling that is present in all dielectric materials, regardless of their atomic or molecular structure. It is a nonlinear effect that relates the electric polarization to the gradient of the electric field and the strain. Mathematically, it is written as Equation 1.15,

$$P_i = \mu_{ijkl} \frac{\partial E_j}{\partial x_k} \frac{\partial \epsilon_l}{\partial x_l} \tag{1.15}$$

where P is the polarization vector, E is the electric field, ϵ is the strain tensor, and μ_{ijkl} is the fourth-order flexoelectric tensor. [10]

This universality of flexoelectricity makes it a highly promising effect for various applications, particularly in micro and nanoscale devices. A comparison between the three phenomena can be seen in Figure 1.3.

One of the key advantages of flexoelectricity is its scalability. Unlike piezoelectricity, which is scale-invariant, flexoelectricity is a size-dependent effect, meaning that it becomes increasingly important as the size of the material is reduced. This makes it ideal for use in micro and nanoscale devices, where piezoelectricity is less effective. Additionally, flexoelectricity can produce larger strains and electric fields than piezoelectricity, making it more efficient for certain types of applications. [12]

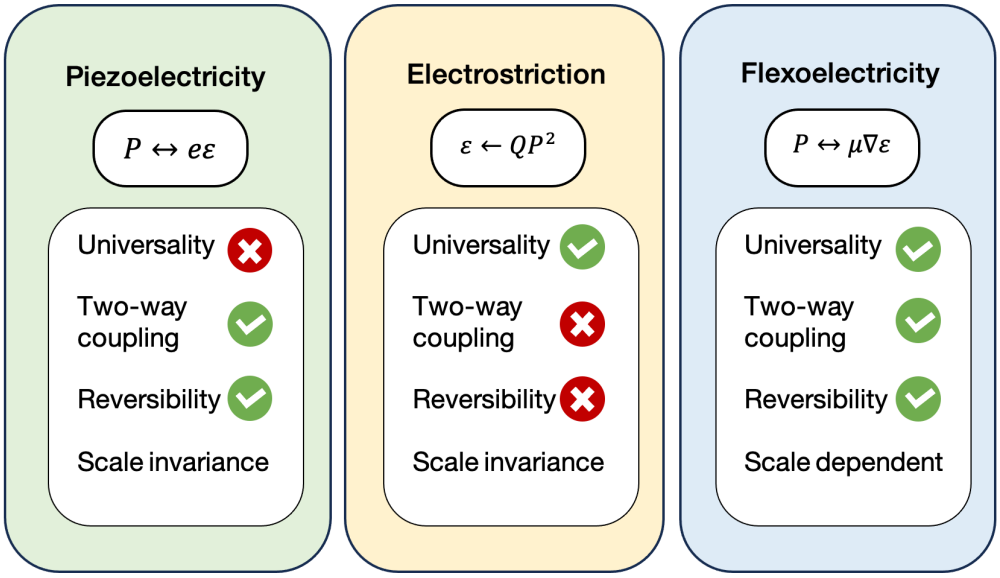

Figure 1.3: *Piezoelectricity, electrostriction, and flexoelectricity are distinct electromechanical phenomena found in various materials. In ionic crystals, piezoelectricity requires a non-centrosymmetric atomic structure, while electrostriction and flexoelectricity are more universal in dielectrics. Flexoelectricity becomes significant at smaller scales, while electrostriction is more pronounced in soft materials. Electrostriction exhibits one-way coupling, while piezoelectricity and flexoelectricity have two-way coupling capabilities. Flexoelectricity is scale-dependent, while piezoelectricity and electrostriction are scale-invariant. Inspired by [11].*

1.4 Thesis goals

The ultimate goal of this project is to design and fabricate a device and material characterization method for the measurement of electromechanical properties of thin films. However, the main goals of the thesis project can be divided into several steps, each contributing to the overall objective of investigating the flexoelectric effect in cantilevers. The project begins by fabricating dielectric microbeams with electrical contacts on two sides to measure the deformation under excitation. The following goals outline the specific steps to be undertaken:

1. Designing a bottom contact: The first step is to design an electrical contact using doping techniques. This contact will serve as a substrate for the dielectric layer and also be tested as an etch stop for microcantilever beam fabrication.

2. Deposition of dielectric layers: The next goal is to successfully deposit multiple layers of dielectric material without compromising the structural integrity of the beams. Ensuring the stability of the structures is crucial for the development of a reliable device.

3. Study on film quality: A comprehensive investigation will be conducted on the quality of silicon nitride thin films to be used in the device. This study aims to assess the

film's properties and suitability for the desired application.

4. Design and implementation of electrical contacts: A fabrication procedure will be developed to create electrical contacts at both the micro and macro scales. The conductivity of these contacts should meet the requirements of the device, and isolation between the contacts must be ensured.

5. Development of a testing system: A testing system will be designed and assembled, focusing on measuring the deformation response of the cantilevers to oscillation voltage applied to the contacts. This system will enable the evaluation of the flexoelectric effect in the fabricated device.

By accomplishing these goals, the thesis aims to advance the understanding and characterization of flexoelectricity and other electromechanical coupling effects.

1.4.1 Device concept

To achieve the characterization of this effect, a system with free-standing cantilevers is designed and fabricated, illustrated in Figure 1.4, which is subjected to either a DC or AC voltage, and the resulting deformation or oscillation is measured.

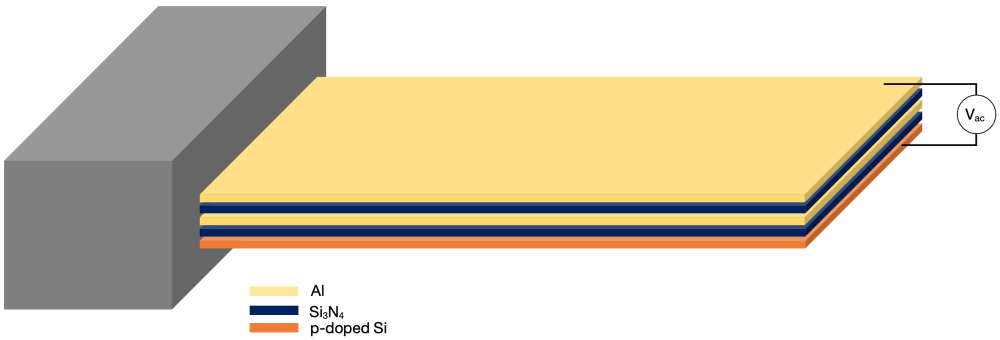

Figure 1.4: *Representation of the cantilever beam fabricated as a stack of materials, seeking to optimize the overall flexoelectric effect. A bottom contact p-doped contact is followed by a silicon nitride dielectric film. To make the system capacitive and enhance the effect, a metallic film needs to be deposited between two of these dielectric ones, followed by a final top contact, made with a Al film.*

One important consideration in the design of the system is the need for an easy way to make two contacts for the cantilever beams. Silicon is chosen as the material for the system, and several different approaches are considered for creating the contacts.

One possibility is to dope a first layer with a very high concentration of dopants, resulting in a material with metallic behavior. This is done as a previous step to RIE (reactive ion etching), which is used to create side windows and underetch the structures to obtain free-standing cantilevers. However, if RIE is not available, an alternative approach needs to be implemented.

It is decided to use the high doping as an etch stop, and boron is found to be more effective than phosphorous as the impurity source.

2 Experimental methods

The following section presents the methods used in this study. These methods include the fabrication physical principles and the most relevant instruments employed. The goal of this section is to provide a clear and concise overview of the procedures and techniques used in the research.

2.1 Anisotropic etching of silicon

The technique of anisotropic etching has been widely studied for its ability to create complex, three-dimensional structures in silicon. While isotropic etching uniformly removes material from all directions, anisotropic etching removes material along specific crystallographic planes or directions faster than along others, as shown in Figure 2.1.

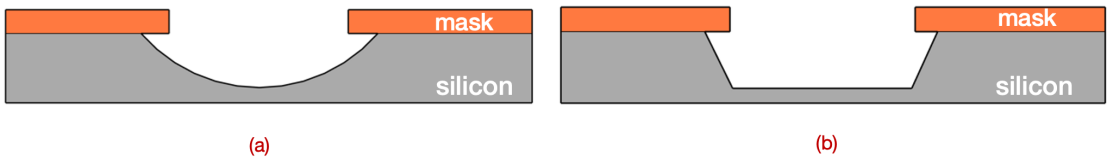

Figure 2.1: *Schematic depiction of the a) isotropic etching and b) anisotropic etching in silicon.*

The etch rate of silicon varies depending on the crystal orientation and the concentration of dopants in the material. This property allows for the design and fabrication of precise structures with consistent etching characteristics.

All anisotropic etchants for silicon are aqueous solutions that contain alkali metal hydroxides, such as potassium hydroxide (KOH) or sodium hydroxide (NaOH). These solutions are either organic or inorganic, but the etching properties are similar regardless of the type of solution used.

The first researchers to propose a mechanism for the etching process were Finne and Klein. Their work laid the foundation for further study and development of anisotropic etching of silicon. [13]

Plane	Surface bond density ($\cdot 10^{15}/cm^2$)	In-plane bond density ($\cdot 10^{15}/cm^2$)	Total bond density ($\cdot 10^{15}/cm^2$)
(110)	0.96	0.96	1.92
(100)	1.36	0.00	1.36
(111)	0.78	0.00	0.78

Table 2.1: *Surface bond density, in-plane bond density and total bond density for the (110), (100) and (111) Si planes. [14]*

2.1.1 Crystal orientation

An electrochemical model has been proposed to explain the anisotropic etching behavior of different crystal planes in alkaline solutions. This model suggests that during the oxidation step, four hydroxide ions react with a single silicon atom on the surface of the crystal, injecting four electrons into the conduction band. These electrons remain localized near the surface due to the presence of a space charge layer. The reaction is accompanied by the breaking of the backbonds, which requires the thermal excitation of surface state electrons into the conduction band. This step is considered to be the rate-limiting factor in the etching process.

In the reduction step, the injected electrons react with water molecules to form new hydroxide ions and hydrogen. It is assumed that the hydroxide ions generated at the surface are consumed in the oxidation reaction rather than those from the bulk electrolyte, since the latter are kept away from the crystal by the negative surface charge. According to this model, monosilicic acid ($Si(OH)_4$) is formed as the primary dissolution product in all anisotropic silicon etchants. The anisotropic behavior is attributed to small differences in the energy level of the backbond surface state, which varies depending on the orientation of the crystal. [13]

The etch rate is dependent on the total number of bonds present on the surface, encompassing both in-plane and surface bonds. Analyzing the surface bond density among the commonly observed {100}, {110}, and {111} crystallographic surfaces reveals notable variations. Specifically, the {100} surface exhibits the highest surface bond density among the three, while the {111} surface exhibits the lowest, as summarized in table 2.1. Conversely, when considering in-plane bond density, the {110} surface stands out significantly, displaying the highest density among the three crystallographic surfaces. For the (110) plane, each atom has both a surface bond and one in-plane. Consequently, the {110} surface has a higher overall bond density compared to the others. This observation aligns with the underlying mechanism, indicating that the {110} planes exhibit the most rapid etching rates when exposed to KOH. [14]

2.1.2 Dopant concentration

The etching rate of silicon can be affected by the concentration of dopants, such as boron, in the material. It has been found that at dopant concentrations below a critical value C_0, the etching rate is independent of the concentration of boron. However, at dopant concentrations higher than $2{\cdot}10^{19}$ cm^{-3}, there is a strong reduction in the etching rate, shown in Equation 2.1. This phenomenon is most effective at low concentrations of KOH.

$$E = k_0[B]^{-4} \tag{2.1}$$

In Equation 2.1, E is the etch rate, k_0 is a constant, and B is the concentration of boron in the material. This equation shows that the etching rate is inversely proportional to the fourth power of the boron concentration.

One model proposed by H.Seidel et al. [15] to explain the etch stop behavior attributes it to the electrical effects of holes rather than the chemical effects of boron. The high dopant concentration makes the width of the space charge layer on the silicon surface much smaller, which allows electrons to be injected into the conduction band by an oxidation reaction. The dissolution of silicon in potassium hydroxide (KOH) is a two-step process. In the first step, electrons are injected into the conduction band of the silicon crystal:

$$Si + 4OH^- \longrightarrow Si(OH)_4 + 4e^-$$

In the second step, the injected electrons react with water molecules to form new hydroxide ions and hydrogen:

$$4e^- + 2H_2O \longrightarrow 4OH^- + H_2$$

The overall reaction can be represented by the following equation:

$$Si + 2H_2O \longrightarrow Si(OH)_4 + H_2$$

This reaction shows that one silicon atom is dissolved to form monosilicic acid ($Si(OH)_4$) and hydrogen gas. However, in this case the electrons are not confined to the surface and quickly recombine with holes from the valence band. As a result, the reduction of water cannot take place and new hydroxide ions cannot be formed at the surface. This leads to a decrease in the etching rate to the forth power, as four electrons are required to dissolve

one atom of silicon. [15]

2.1.3 Etch stop method

This thesis focuses on utilizing anisotropic etching of silicon to establish an etch stop, where test samples along the (001) and (011) planes were designed to evaluate their respective etching rates. To achieve free-standing cantilevers via wet etching in KOH, the implementation of an etch stop becomes crucial. Thus, after defining the desired structure regions using a resist mask, spin-on doping (SOD) with a Poly Boron B153 solution from FILMTRONICS was employed using a POLO spin coater at 2000 rpm for 30 seconds. This process was repeated four times to ensure sufficient boron concentration on the sample surface. Subsequently, the solution-coated sample was cured at 100°C and 175 °C for 30 minutes each. Finally, the sample underwent boron diffusion into the specific areas by placing it in a Nabertherm tube furnace under an Ar atmosphere at 1100°C for 1 hour.

2.2 Micro- and Nanolithography

In this thesis, photolithography and electron beam lithography have been used to produce the studied structures. These are two fundamental techniques that enable the precise patterning of structures with feature sizes ranging from nanometers to millimeters. These, integrated with deposition and etching processes, facilitate the fabrication of micro- and nanoscale architectures.

Masked lithography, including photolithography, employs masks or molds to transfer patterns uniformly over a large area, facilitating high-throughput fabrication. Conversely, maskless lithography techniques such as electron beam lithography operate without the need for masks. These techniques offer the best resolution, which enables the patterning of complex shapes.

2.2.1 Electron beam lithography

Electron beam lithography is a powerful technique in micro- and nanolithography that utilizes an accelerated electron beam to expose an electron-sensitive resist. The electron beam, focused to a diameter as small as a few nanometers, is scanned across the resist surface in a dot-by-dot fashion, enabling the creation of intricate patterns with exceptional resolution. The sequential exposure initiates interactions that induce changes in the resist, leading to selective removal of exposed or unexposed regions through subsequent processing steps. [16] The process is illustrated in Figure 2.2, in which the experimental setup of the litographical process can be seen.

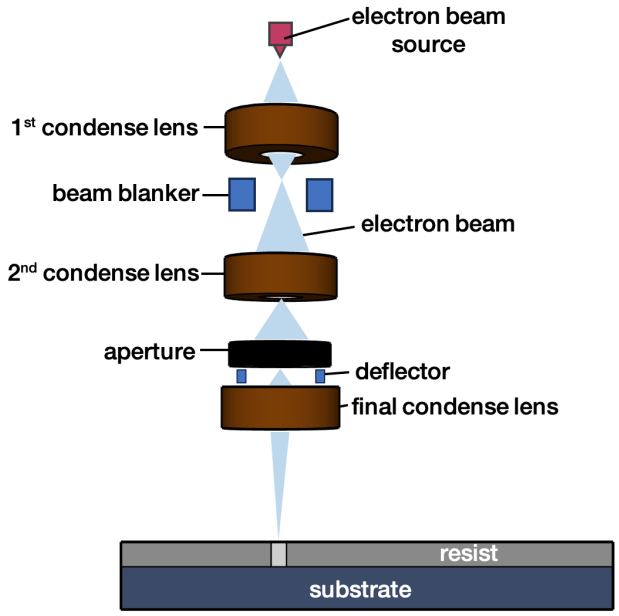

Figure 2.2: *Lateral view on a electron beam writing system, where an electron beam, generated by an electron beam source, is focused by a scanning electron microscope to expose certain parts of an electron-sensitive resist. Inspired by* **[16]**.

The Zeiss EVO 60 scanning electron microscope (SEM) is used for electron beam lithography (EBL). In this process, PMMA is used as a positive resist, i.e., the areas exposed to a certain dose can be removed using a developer leaving the non-exposed areas untouched.

After placing the sample in the SEM, the software Elphy Plus is used to establish a local coordinate system for the wafer, and the electron beam current measured in order to set a suitable exposure time. Templates are designed for the cantilevers and contact pads to be written. Before the procedure, writing zones of 100 by 100 um and 1 mm by 1 mm need to be created and calibrated so as to stitch the cantilever structures to the elongated contact pads.

2.2.2 Photolithography

Photolithography, a widely utilized technique in the semiconductor and integrated circuit (IC) industry, has played a pivotal role in the manufacturing of ICs, microchips, and commercial microelectromechanical systems (MEMS) devices. This versatile method involves the utilization of ultraviolet (UV) light exposure on a light-sensitive polymer known as photoresist to define precise patterns.

In the photolithography process, UV light with wavelengths typically ranging from 193 to 436 nm is directed through a photomask, which comprises opaque features on a

transparent substrate such as quartz or glass. This masked UV light exposure is projected onto a substrate coated with photoresist. Upon exposure, the polymer chains within the photoresist undergo a breakdown, rendering them more soluble in a chemical developer solution. Subsequently, the exposed photoresist is selectively dissolved, removing the undesired areas and leaving behind the desired photoresist pattern on the substrate. [16] The process, both before and after developing the photoresist, can be seen in Figure 2.3.

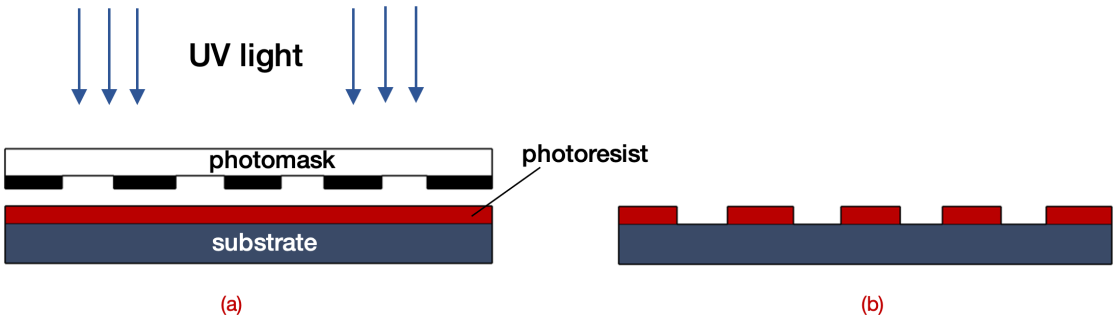

Figure 2.3: *Schematic representation depicting a) exposure process of the photoresist to UV light, using a photomask to define the resist regions to be exposed, and b) the developing of the resist, removing the exposed regions if it is a positive resist and removing the un-exposed regions if it is a negative-type one.*

MICROPOSIT^{TM} S1813^{TM} G2, a positive photoresist, is used in this work. The mask is designed and printed, and the photoresist is spun at 500 rpm for 15 seconds, and then at 4000 rpm for a period of 30 seconds. Once the spinning process is complete, the photoresist-coated substrate is transferred to a hotplate heated to a temperature of 110°C. The photoresist is subjected to the heat for 60 seconds. The sample is then placed, partially covered by the photomask, in a UV source for 3 minutes. The patterns are developed using a mr-Dev 600 solution. Right after, the samples are rinsed with DI water and dried.

2.3 Deposition techniques

2.3.1 Electron beam evaporation

Electron beam deposition is an advanced method for creating thin films by evaporating materials using high-energy electrons within a vacuum environment. It offers superior control and produces high-quality films with minimal defects. Compared to traditional heating methods, electron beam deposition eliminates contamination issues and enables precise deposition of thin films with various materials.

Electron beam evaporation offers advantageous characteristics for lift-off processes due to its inherent directionality, minimizing sidewall coverage. Notably, compared to

thermal evaporation, e-beam evaporation allows for a higher input of energy into the source material. As a result, films with increased density and enhanced adhesion to the substrate are achievable. Moreover, the localized heating of the source material by the electron beam, rather than the entire crucible, reduces contamination from the crucible, making it a preferable option. Multiple crucible E-beam guns enable the deposition of various materials without breaking the vacuum. The process involves heating a filament beneath the crucible and applying a high voltage to draw electrons from the filament. These electrons are then focused into a beam through bending magnets and swept across the surface of the source material, uniformly heating it. A quartz crystal is present in the chamber to monitor the amount of material deposited. [17]

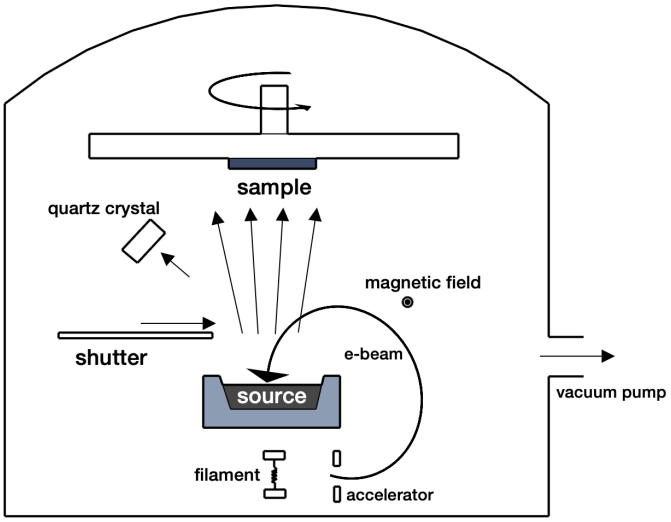

Figure 2.4: *Schematic representation of an e-beam evaporation system. The sample is rotating continuously to ensure homogeneous deposition. Inspired by [18].*

In this thesis, the Flextura 200 system is used to deposit chromium and silver layers for the device electrical contacts.

2.3.2 Reactive magnetron sputtering

Within a magnetron sputtering deposition system, several components facilitate the process: a sample holder positioned below a heater, a quartz resonator crystal, a magnetron, and a target composed of the material to be sputtered. The basic principle can be seen in Figure 2.5. By activating the magnetron, argon (Ar) gas is introduced, and a voltage is applied between the target and an electrode. This voltage causes ionization of the Ar gas, resulting in positively charged ions that accelerate toward the cathode (target). The high energy of these incoming ions dislodges atoms from the target, as well as generates secondary electrons. To enhance plasma sustainment, permanent magnets

positioned behind the target guide the electrons along a helical path through the Ar gas, increasing collision probability. In a reactive system, a shutter is employed to prevent material deposition on the sample until the process stabilizes. Once stability is achieved, a controlled flow of the desired reactive gas is introduced. Subsequently, when the shutter is removed, thin film growth commences. [19]

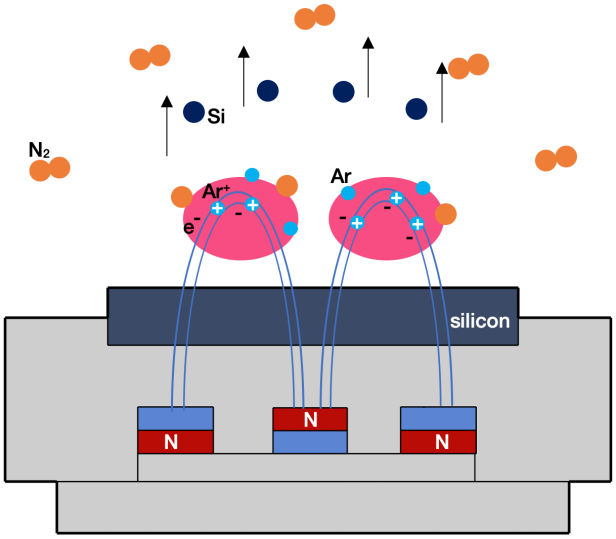

Figure 2.5: *Schematic representation of the functioning principle of a magnetron sputtering deposition system. Inspired by [19].*

The growth of thin films on the cantilever structure is achieved through the utilization of reactive DC magnetron sputtering. This process is conducted using the advanced Flextura 200 system, which is purposefully designed and manufactured by Polyteknik A/S. The sputtering process involves both reactive and normal modes of operation, wherein the deposition of silicon nitride films requires the utilization of nitrogen gas in the reactive mode, while the normal mode is suitable for aluminum film deposition.

3 Device: Nanofabrication Results and Discussion

3.1 Fabrication process

The samples fabricated in this thesis project will be cantilever beams. In search of a recipe that optimizes, in this case, the flexoelectric effect, firstly, a set of cantilever beams and other structures will be fabricated to test the optimal parameters to obtain heavily doped, free-standing beams. Secondly, a dielectric Si_3N_4 thin film will be introduced in a second set of cantilever beams. Lastly, the finished cantilever beam system will be built as a stack of dielectric layers separated by electrical contacts. To this end, this chapter will introduce the methods employed to both fabricate and characterise the samples. For the sake of brevity, each optimization step will not contain the numerous previous attempts that failed if it is not of relevance to the results and conclusions of this project.

3.2 Step I: Fabrication of the cantilever structures

The fabrication process, illustrated in Figure 3.1, begins with a silicon (100) wafer with a 300 nm SiO_2 film serving as the substrate. A 100 nm film of PMMA (poly(methyl methacrylate)) is spin-coated onto the substrate, and the desired patterns are patterned onto the PMMA film using e-beam writing. The PMMA is then developed, leaving behind the patterned PMMA film.

In the conventional approach, the fabrication process involves using reactive ion etching (RIE) after e-beam lithography to pattern the oxide mask. This technique ensures improved etch anisotropy by vertically accelerating the ions, minimizing lateral etching [20]. However, due to the unavailability of RIE, an alternative method had to be employed. In this case, the patterning of the oxide mask for selectively doping the structures is accomplished using HF wet etching. Therefore, the SiO_2 film is etched, leaving behind the patterned SiO_2 film. The PMMA mask is then removed with acetone.

A coat of Boron solution is then applied to the sample and spin-coated, resulting in a uniform layer of boron on the surface of the sample. The sample is placed in a tube furnace at a temperature of 1100°C and subjected to a thermal drive-in process for 1

hour in a Ar atmosphere. This process causes the boron to diffuse into both the Si and the SiO_2 films, resulting in the selective doping of the silicon cantilever structures.

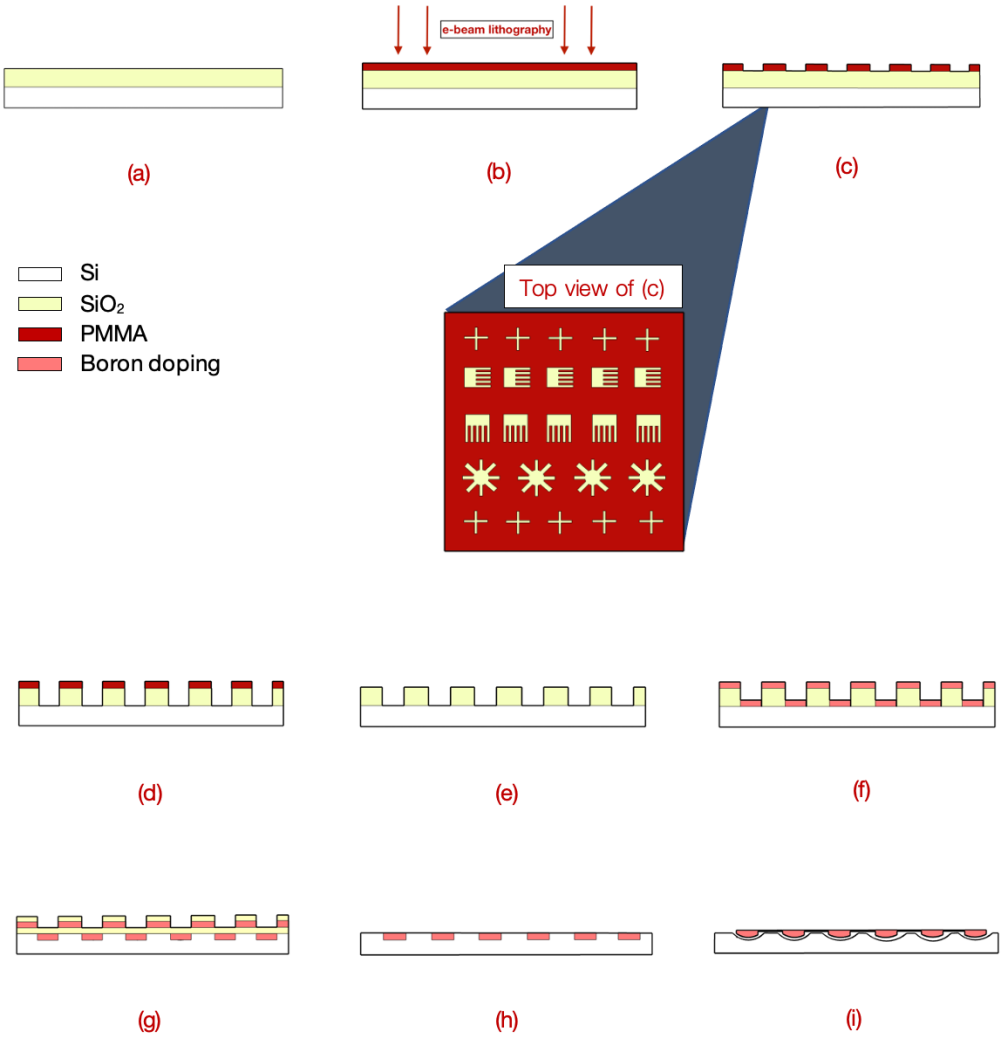

Figure 3.1: *Nanofabrication process of the cantilever beams and test structures. a) Substrate is a silicon (100) wafer with a 300 nm SiO_2 film. b) A 100 nm film of PMMA is spin-coated and the desired patterns are patterned by e-beam writing. c) The PMMA is developed. d) Using the remaining PMMA pattern as a mask, the SiO_2 is selectively etched. e) The PMMA is removed with acetone. f) A coat of Boron solution is applied to the sample and spin-coated. g) At a tube furnace at 1100°C, the boron is "driven-in" for 1 hour in Ar atmosphere. h) All remaining SiO_2 is etched in HF. i) The beam structures are liberated from the wafer by anisotropic etching with KOH.*

Finally, all remaining SiO_2 is etched away using HF (hydrofluoric acid), and the beam structures are liberated from the wafer by anisotropic etching with a 10% wt. solution of

KOH (potassium hydroxide) for 90 minutes at 50°C. This last step ensures a slow etching of the silicon, which enhances the etch stop effect.

3.3 Step I results: Cantilever formation

The results of the cantilever beam formation experiment reveal that the beams have undergone significant widening during the thermal drive-in process and subsequent etching. This is evident when comparing Figures 3.2 and 3.3, which show that the beams' width increased from approximately 1.5 microns after e-beam writing to 5 microns after the completion of the entire process. This expansion is believed to be a result of the permeation of boron under the oxide mask.

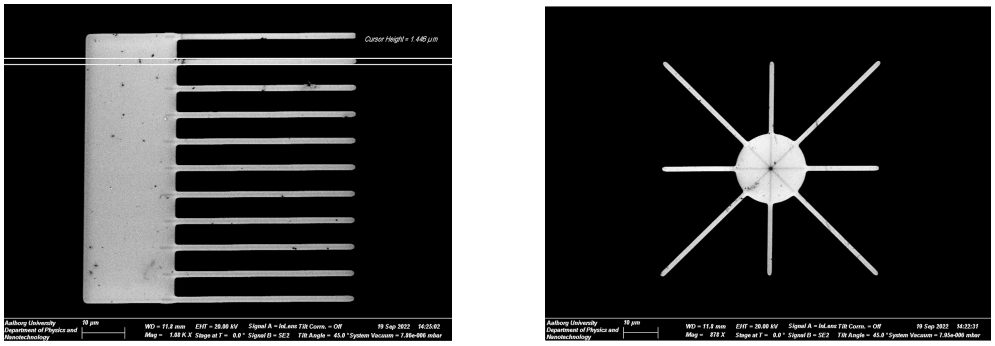

(a) (b)

Figure 3.2: *SEM images of a) Hair comb-like structure developed in PMMA after e-beam exposure. Cantilever structure width is measured to be 1.446 microns before cantilever formation. b) Ring-like structure developed in PMMA after e-beam exposure. Cantilevers are placed at 90° and 45° from each other to test the dependence of crystallographic planes in etching.*

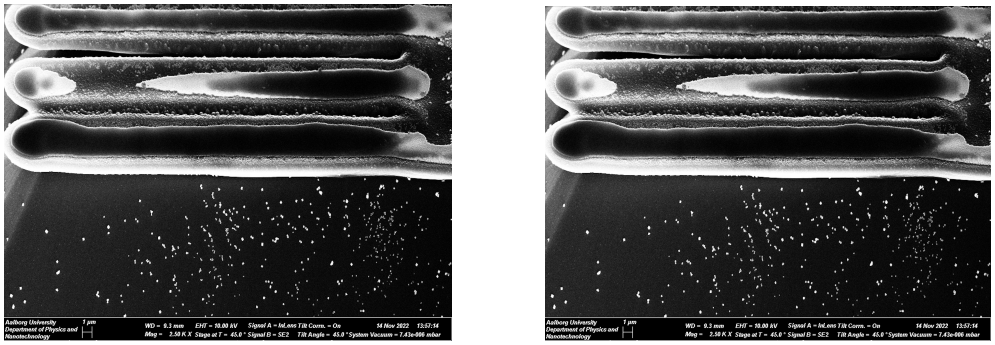

(a) (b)

Figure 3.3: *SEM images of a) After-etching cantilever structures in the hair-comb version. The beams have widened to around 5 microns. b) Unreleased beams in the (001) plane of the wafer.*

Additionally, it was observed that only specific crystallographic orientations of the beams were successfully released and are now free-standing, specifically those on the (011) plane of the Si(100) wafer, as depicted in Figure 3.4. The results indicate that the (011) plane etches faster than (001), as evidenced by the unreleased beams seen in Figure 3.3. Furthermore, it was discovered that a remaining SiO_2 film, observed in Figures 3.3 and 3.4, had to be etched multiple times to fully remove it from the structures. This is most likely due to the boron-doped regions making the film slightly etch-resistant to HF, as the rest of the wafer was SiO_2 free.

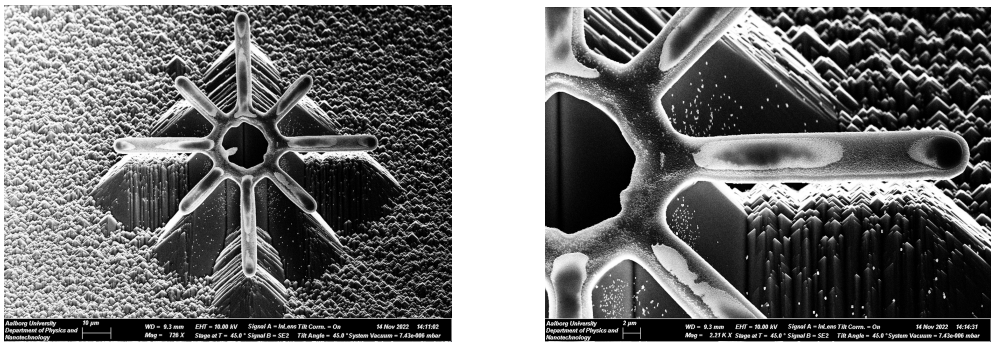

(a) **(b)**

Figure 3.4: *SEM images of a) Ring-like cantilever structure after etching. b) Zoom-in of the only orientation in which the beams are completely free-standing, the (011) plane.*

Above, the behavior of the beams during the e-beam writing and etching processes is discussed. It is observed that the beams undergo a widening from approximately 1.5 μm in the exposed regions during e-beam writing to around 5 μm in the released structures after the completion of the etching process. This widening is attributed to the spin-on-doping process, which is carried out with the protection of the e-beam resist. Subsequently, the structures are subjected to a drive-in process where they are heated to 1100 °C for 1 hour. During this process, boron diffuses into the silicon in the exposed regions of the mask. However, it is noted that the diffusion process is not entirely directional, resulting in a slight lateral diffusion along with the vertical diffusion. Consequently, the doped area that will be protected against KOH etching is slightly increased.

The etching process is tested multiple times using various doping doses and experimental conditions. Since the boron concentration in the doping solution is unknown, it takes four rounds of spin coating the solution on the sample to reach the critical value as described by Equation 2.1, which describes the relation between the boron concentration to the etching rate. It is crucial to maintain the etch rate at approximately 20 nm/min to achieve the desired etch stop effect. This is accomplished by using a 10% KOH solution at a temperature of 50°C.

Overall, these findings provide insights into the behavior of the beams during the e-beam writing, spin-on-doping, and etching processes. The observations of beam widening and the diffusion of boron during the drive-in process contribute to the understanding of the fabrication steps. The multiple tests of the etching process under different conditions emphasize the importance of achieving the appropriate etch rate and critical boron concentration for successful etch stop effects.

3.4 Step II: Addition of a Si_3N_4 layer

Silicon nitride is the chosen dielectric material for a thin film system on silicon cantilever beams for flexoelectricity measurements. Its properties, such as its wide bandgap, high dielectric constant, high thermal stability, chemical stability, and flexibility make it an ideal material for this application. The wide bandgap of Si_3N_4 makes it less susceptible to leakage currents, which can interfere with the measurement of flexoelectric properties. Its high dielectric constant enhances the flexoelectric effect, allowing for more sensitive measurements. The high thermal stability of Si_3N_4 allows for measurements to be made at elevated temperatures, which can be useful for some applications. Additionally, its chemical stability makes it resistant to chemical attack and corrosion, making it suitable for use in harsh environments. Lastly, its ability to be deposited in thin films allows for the characterization of the flexoelectric effect, providing accurate and precise measurements. [21].

Residual stress in thin-film materials refers to the presence of an internal stress state without any external forces, which can be either compressive or tensile. While various material properties of deposited thin films are influenced by specific processing conditions, residual stress often exhibits significant variability. It is not uncommon for residual stresses in thin films to span a wide range of values, sometimes exceeding 100%, and even change from compressive to tensile states. Several factors contribute to the formation of residual stress, including deposition conditions, the materials involved (both thin films and substrates), and subsequent processing steps involving elevated temperatures. Understanding the origins of residual stress is complex and multifaceted, and as a result, there is currently no universally applicable theory to predict residual stresses in thin films. Processes like sputtering deposition, which involve energetic bombardment of thin film surfaces, can introduce interstitials that contribute to built-in compressive intrinsic residual stresses. Additionally, in reactive sputtering, the final composition of the film can lead to lattice mismatches with the substrate, resulting in either tensile or compressive strains. When the thin-film atoms bond with the exposed atoms of the substrate, mismatches in lattice constants can cause the atomic bonds to be strained, leading to either stretching or compression. [22]

In order to minimize strain and ensure that the cantilevers do not bend or break, a study on the effect of nitrogen concentration need to be carried out. A silicon target is utilized in the Flextura magnetron sputtering deposition system, which is operated in an atmosphere of Ar and N_2. Four tests are conducted to evaluate the films' quality and stress, utilizing a profilometer and ellipsometer for characterization. The quality of the film is determined by assessing its stress and comparing it to an ellipsometric model. To ensure consistency, the initial settings for the tests include a room temperature and a power of 300 W. The argon-nitrogen flow ratio is then gradually modified, starting from 9:9 and ending at 9:3, shown in Table 3.1.

In order to analyze the residual stress introduced to the sample, measurements conducted with a profilometer can be examined using Stoney's equation. Specifically, for (100) wafers, the equation is given as:

$$\sigma_f \frac{t_f}{M_{Si}(001)h^2} = \frac{1}{6}\left(\frac{1}{R_{\text{post}}} - \frac{1}{R_{\text{pre}}}\right) \tag{3.1}$$

where $M_{Si}(001) = 1.803 \times 10^{11}\,\text{Pa}$ represents the biaxial modulus, h denotes the thickness of the substrate, and t_f corresponds to the thickness of the film [55]. The curvature radii of the wafers before and after the deposition, R_{pre} and R_{post}, can be approximated by the following equation when $L \gg B$:

$$R = \frac{L^2}{8B} \tag{3.2}$$

Here, L signifies the scan length during the profilometer measurements, which was consistently set at 4 mm for all measurements, and B represents the bow, which denotes the maximum absolute value of the measured bow. If the difference between R_{post} and R_{pre} is negative, it results in a negative value for stress, indicating compressive stress. Conversely, positive stress values indicate tensile stress [23, 24].

Sample	**Ar:N_2 Ratio**	**Thickness (nm)**	**Residual stress (MPa)**
S1	9:9	-	-
S2	9:6	170	3.75
S3	9:4	207	0.74
S4	9:3	255	-1.16

Table 3.1: *Different test samples for a rapid silicon nitride film deposition optimization. It can be seen that S1 yields no measurable film, and that stress decreases from compressive stress in S2, to S3, and then tensile stress increases in S4.*

All four test depositions are performed for a duration of 20 minutes. The 9:9 ratio does not yield any measurable film, thus the ratio is adjusted to 9:6, resulting in the production of a 170 nm silicon nitride film after 20 minutes. Two additional tests are conducted

with ratios of 9:4 and 9:3. Both yield similar films, but the 9:4 ratio exhibits the lowest stress levels. The 9:3 ratio, on the other hand, shifts from tensile to compressive stress, with increasing levels as the ratio increases. Additionally, the 9:4 ratio aligns perfectly with the ellipsometric model for silicon nitride. This ratio is deemed sufficient for film optimization and is subsequently tested on a cantilever test structure.

3.5 Step II results: Si_3N_4 layer addition

The cantilever test structure, consisting of free-standing beams, is employed for depositing the silicon nitride film. The sample is placed in the sputtering system for a duration of 20 minutes, resulting in the deposition of approximately 200 nm of silicon nitride. The sample is then examined using a scanning electron microscope (SEM) to assess whether the beam structure has been affected in any way due to the inevitable strain caused by the lattice mismatch between the two materials. However, as illustrated in Figure 3.5, the cantilever beams are fully covered by the silicon nitride film and their structure remains intact. Two different microstructures can be seen on the beams, as there is an underlying layer of silicon oxide that was not completely removed prior to the test deposition of the silicon nitride. In that way, it can be seen that the new nitride shows the microstructure of the underlying silicon in the outer edges and silicon oxide in the centre. This was fixed for the final structures, which have been etched thoroughly and have no remaining oxide.

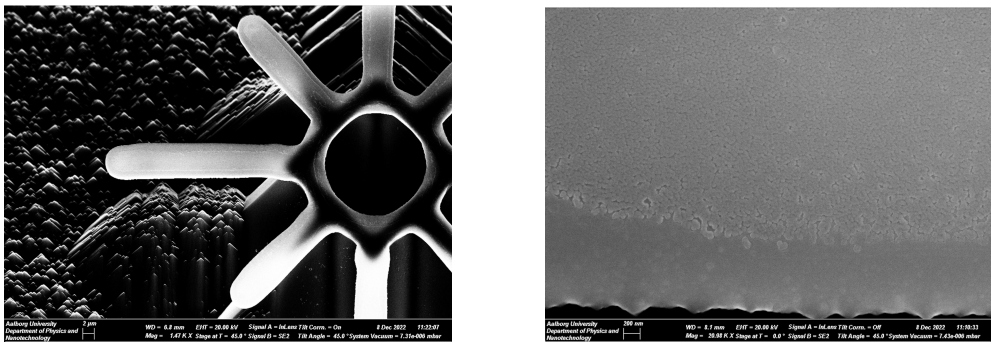

(a) **(b)**

Figure 3.5: *SEM images of a) Free-standing cantilever coated with a 200 nm silicon nitride film. b) Film grain structure. Although an underlying SiO_2 film remains, the silicon nitride film is continuous and homogeneous throughout the sample.*

It has been observed that higher nitrogen concentrations are associated with an increase in compressive stress. This trend is supported by the findings of Liu et al. [25] and D.L. Ma et al. [26]. Both studies attribute the increase in compressive stress to changes in ion bombardment during the deposition process. According to D.L. Ma et al., an increasing

ion-to-neutral rate of aluminum and silicon in front of the substrate, resulting from higher nitrogen flow, leads to a higher intensity of ion bombardment, thereby increasing compressive stress. Liu et al. concluded that the growing number of defects, accompanied by the intensifying ion bombardment, contributes to the increase in compressive stress [25, 26]. Figure 3.6 visually illustrates this phenomenon, as the Ar:N_2 ratio indicates a shift towards compressive stress with higher nitrogen content. Notably, a 9:3 Ar to N_2 ratio exhibits a lower nitrogen concentration, allowing for a switch to tensile stress. One possible explanation for this observation could be the activation of the metal mode, leading to predominantly silicon deposition.

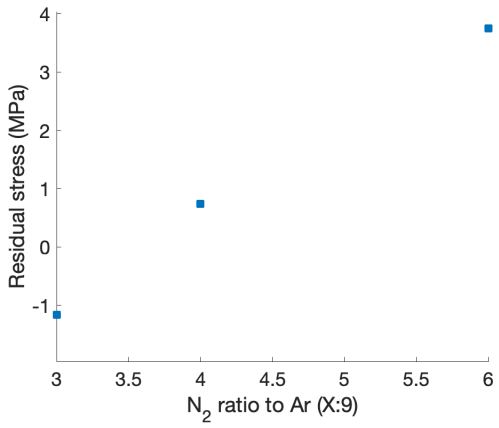

Figure 3.6: *Residual stress as a function of nitrogen ratio in respect to argon during the sputtering process. Very low nitrogen concentrations produce tensile stress, while very high concentrations increase compressive stress in the film.*

3.6 Step III: Contact layout and film stacking

In designing the contact layout for the cantilever beams, several factors must be taken into account. The etched layout structure, illustrated in Figure 3.7, is entirely p-doped, and will serve as the bottom contact for the device before the deposition of the dielectric film system and subsequent application of a metallic Al top contact.

To ensure proper functionality, the bottom contact must be separated from the measurement structure. To achieve this, a 1 mm writing field will be established in the e-beam writing software and stitched to the 100 micron field where the cantilever structure is written. The top contact will be designed as a circle attached to the beams, with a diameter of 80 microns to accommodate a contact needle. To protect the bottom contact during subsequent fabrication steps, it will be designed to be 100 by 200 microns in size, and will be easily identifiable under an optical microscope for precise alignment. It will

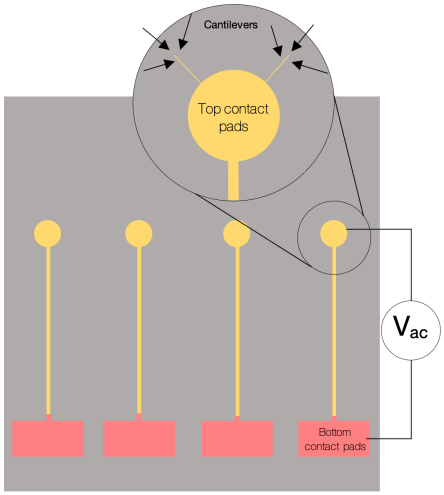

Figure 3.7: *Representation of the contact layout design. In yellow, the Al top contact, and in pink, the exposed p-doped pad of the cantilever's bottom contact.*

be covered during the deposition of the dielectric film system and other fabrication steps and will be uncovered at the end of the process shown in Figure 3.8.

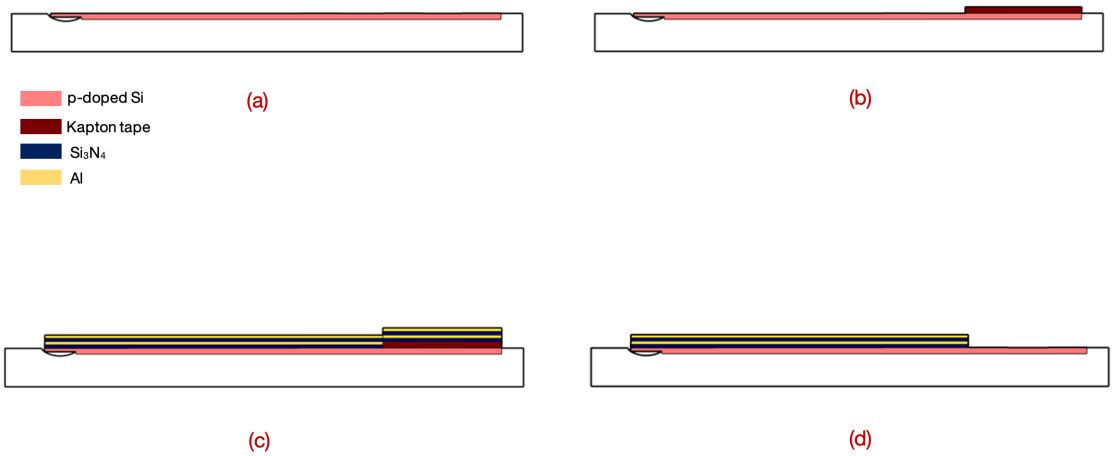

Figure 3.8: *Nanofabrication process of the addition of the contact pads. a) Substrate is a silicon (100) wafer with a free-standing cantilever structure and elongated p-doped region for the contact pads strcuture. b) Using Kapton tape, the a part of the structure is masked to protect it from the subsequent steps. c) The stacked films are deposited on the entire sample, ending in a metallic Al top contact. d) The tape is removed to expose the bottom contact pad.*

3.7 Step III results: Final beam structures

In Figure 3.9, SEM images of the etched final layout structures are shown. In these, both the boron-doped contact structures and the 20 micron long beams can be seen.

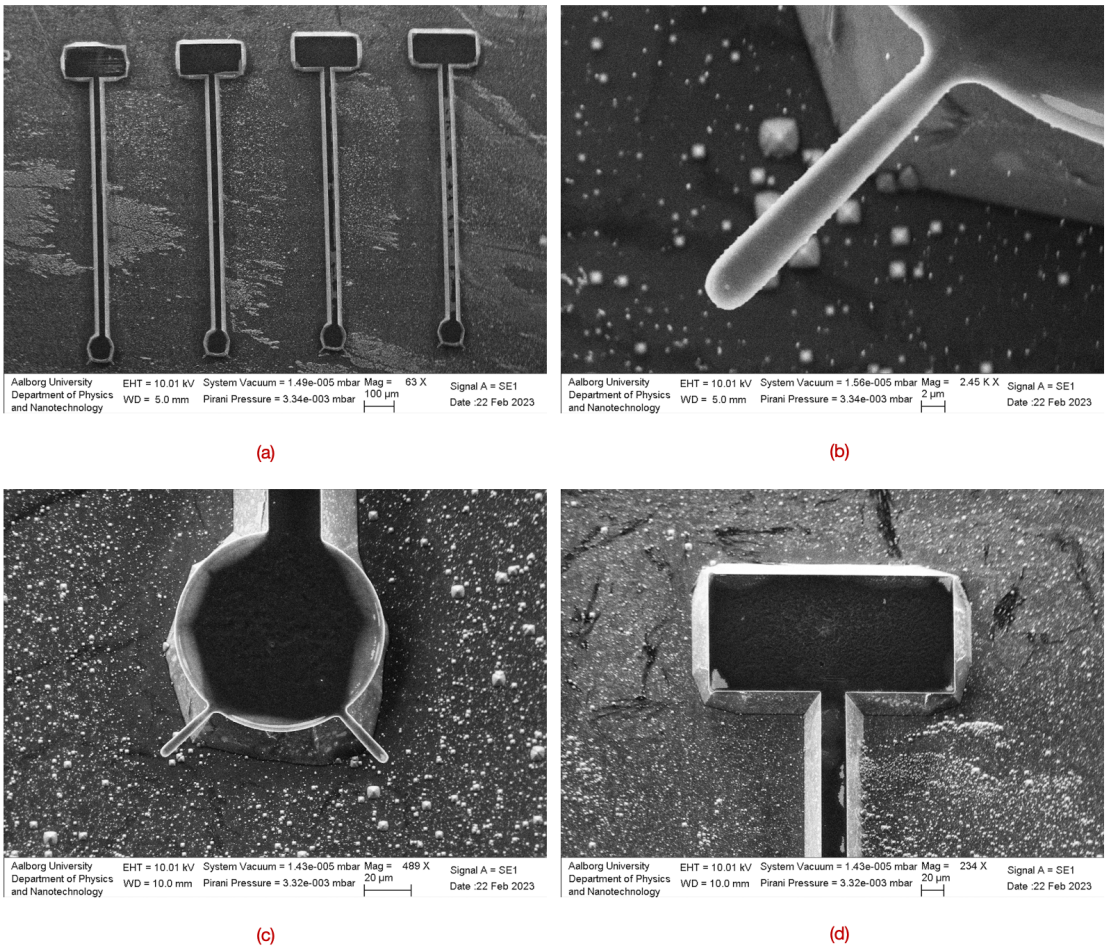

Figure 3.9: *SEM images of the doped-silicon base contact structure, before the films deposition. a) Full base structure, showing both the future bottom (rectangular) contact and top (circular) contact and the beams attached to this last one. b) Beam structure, of around 4 microns in width and 20 microns in length. c) Zoom-in on top contact structure, with two beams in the (001) plane of the used Si(100) wafer. d) Zoom-in on bottom contact structure.*

3.7.1 Film stacking

Numerous dielectric materials have been investigated in the context of flexoelectricity. Despite the utilization of materials with high flexoelectric coefficients, macro-scale sensors employing flexoelectricity generally demonstrate lower sensitivities compared to their piezoelectric counterparts. To address this issue of low sensitivity, a common approach involves the development of a multilayered structure, wherein multiple flexoelectric layers are stacked to amplify the effect. [27]

The stacking procedure is conducted using the same magnetron sputtering system that was employed for depositing the silicon nitride film. For characterization purposes, a test sample is utilized, and a layer stacking consisting of silicon nitride-aluminum-silicon nitride-aluminum is deposited.

To determine the thickness of each film in the stack, the cross-section of a test sample is examined under a scanning electron microscope (SEM). The SEM analysis reveals a consistent thickness of 200 nm for each film, as depicted in Figure 3.10b. These measurements serve as a reference for the subsequent deposition of the film stack onto the actual cantilevers.

Furthermore, Figure 3.10a displays the microstructure of the top aluminum film, providing a visual representation of its surface characteristics. This microstructure analysis offers valuable insights into the quality and morphology of the deposited aluminum layer, which can be seen to be crystalline and homogeneous.

As previously mentioned, Kapton tape is utilized for masking, as depicted in Figure 3.11a. The tape is applied to precisely define the desired region for the bottom contact.

Figures 3.11b and 3.11c provide visual representations of the tape removal process and its impact on the sample. It is observed that the removal of the tape results in a well-defined and sharp edge, indicating the successful masking procedure. However, there is a slight shadowing effect visible, suggesting that some material may have seeped under the tape during the sputtering process.

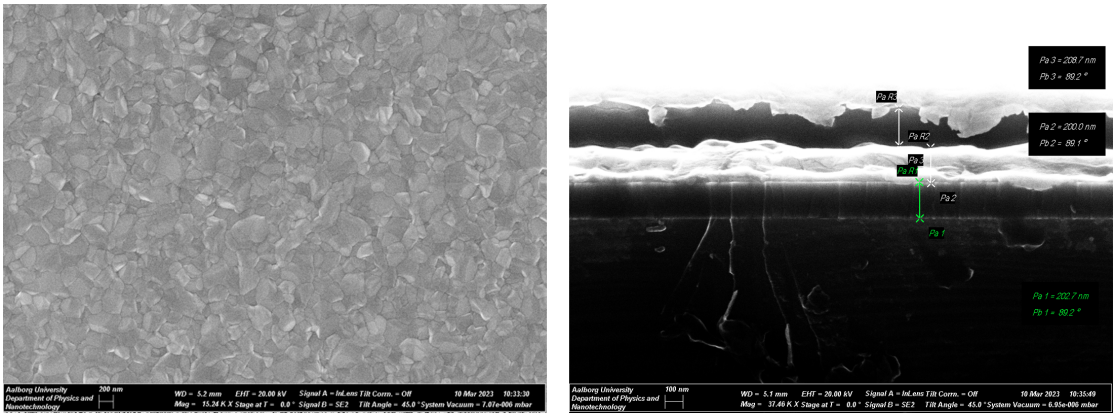

(a) (b)

Figure 3.10: *SEM images of a) microstructure of the top aluminum film in the stacking and b) the cross-section of a test sample, which reveals a consistent thickness of 200 nm for each film.*

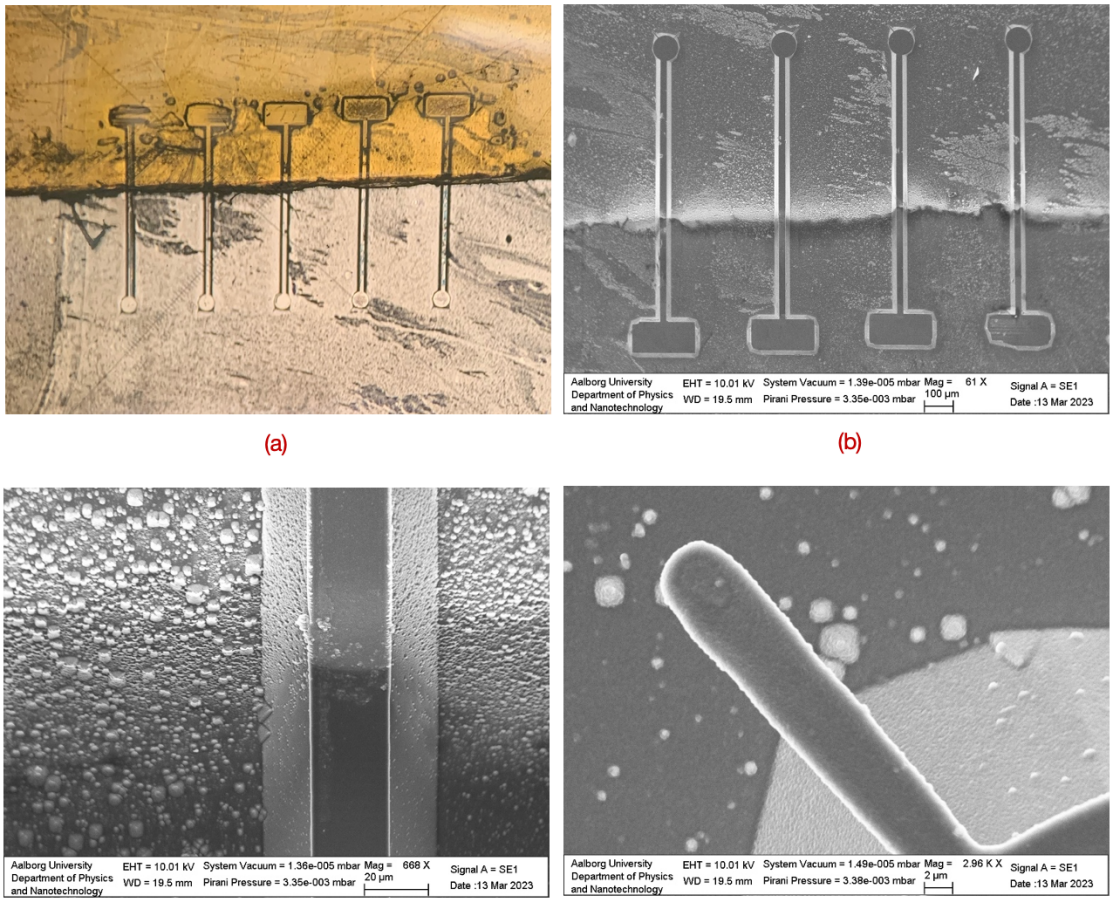

(a) (b)

(c) (d)

Figure 3.11: *Series of images depicting the bottom contact masking process and results. a) Optical microscope image of the Kapton tape mask previous to the deposition of the films. b) SEM image of the masking edge between top and bottom contact regions. c) Zoom-in SEM image of the region in the bridge of the structure where the contacts switch from top to bottom. It can be seen that the change is not very abrupt, indicating a possible deposition of material under the mask. d) SEM image of one of aluminum covered free-standing cantilever beams.*

3.7.2 Contact testing

For the characterization and testing of the contacts, a Süss MicroTec probe station was used.

Initially, the probes were placed on different sections of the aluminum film to evaluate its conductivity. Since the cantilevers are free-standing while the bridge and the connecting circle are not, the deposition of the stacked films is consistent across the entire top-contact region. A voltage linear sweep ranging from 0 to 0.1 V was applied to the aluminum film. The results, shown in Figure 3.12, indicate good and linear conductivity with a maximum current of 16.5 mA at 0.1 V. This suggests that the aluminum film is homogenous and conductive, validating its suitability as a top contact.

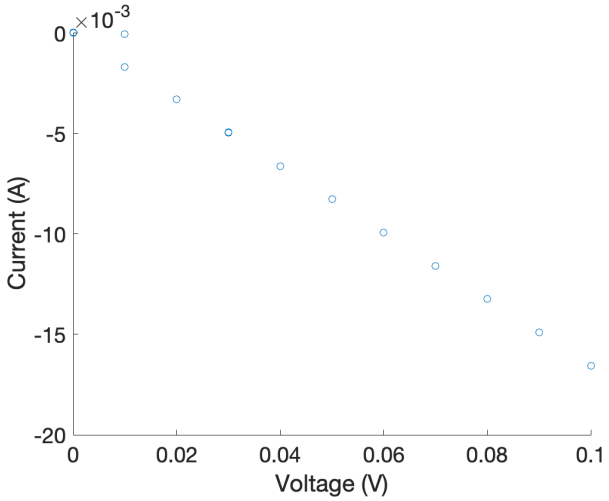

Figure 3.12: *Linear behaviour of the current vs. voltage difference curve for the conductivity test of the aluminum contact.*

Subsequently, the probes were positioned on the doped silicon bottom contact, as illustrated in Figure 3.13a, to assess its viability as a contact. The measurements revealed a slightly non-linear behavior at low voltages and Ohmic behaviour at higher voltages, with some hysteresis and a maximum current of 0.71 mA at 0.1 V, as demonstrated in Figure 3.13b. Although the doped silicon appears to be less conductive compared to aluminum, it can still function as a contact. This discrepancy is likely attributed to the presence of a few nanometer-thick oxide layer resulting from the treatment with KOH, which increases the resistance of the doped film, approximately equal in thickness to that of the cantilever.

Furthermore, the isolation between the bottom and top contacts was examined, as depicted in Figure 3.14a. The measurements indicated a maximum conductivity drop of 15 μA at 0.1 V, as shown in Figure 3.14b. However, the sweep still exhibited a non-linear I-V

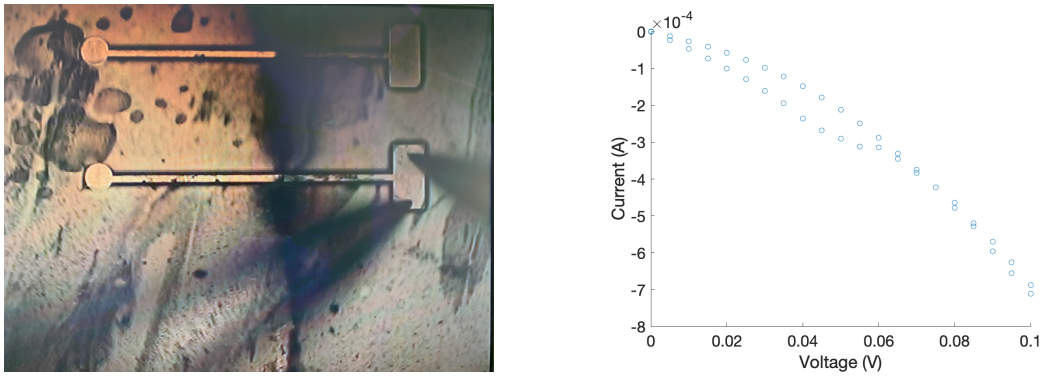

(a) (b)

Figure 3.13: *Conductivity test through a voltage sweep for the doped silicon bottom contact. a) Optical microscope image of the probing setting for the Si-Si contact. b) Slightly non-linear response at low voltages and L linear response at higher ones of the current to a voltage sweep for the doped silicon contact pads, some hysteresis can be seen, but the current still increases linearly.*

characteristic, implying some degree of conductivity between the contacts. This suggests a leakage issue, possibly caused by aluminum deposition under the tape in certain regions of the sample. As sputtering is not highly directional and material can be sputtered from multiple angles, this contact fabrication method is not suitable for successful beam contacting. An alternative approach will be presented in the future perspectives section of this thesis.

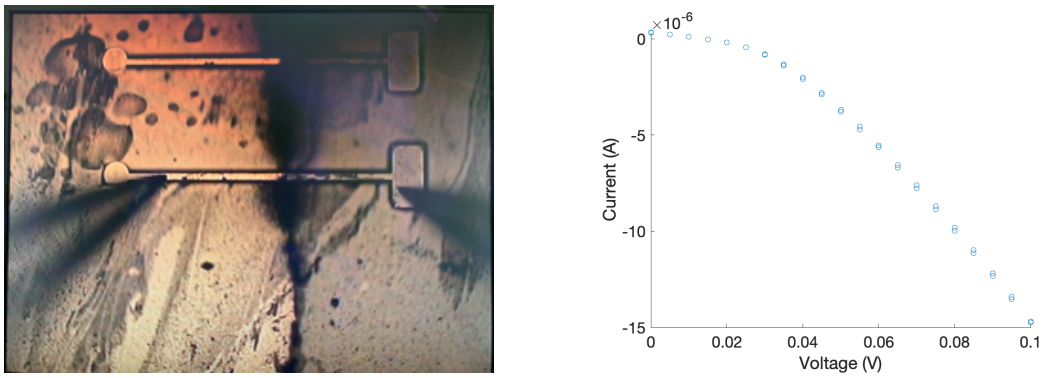

(a) (b)

Figure 3.14: *Conductivity test through a voltage sweep between the aluminum and doped silicon contacts. a) Optical microscope image of the probing setting for the Al-Si contact. b) Non-linear response of the current to a voltage sweep in between the aluminum and doped silicon contacts, when no current is expected, revealing a leak in the fabricated design.*

Regarding the previously seen step in the bottom - to - top contact separation seen

in Figure 3.11b and 3.11c, the presence of a shadowing effect signifies the need for further optimization of the masking technique to minimize any unintended material deposition in the masked region. It is crucial to achieve precise masking to ensure the desired configuration and functionality of the bottom contact in the fabricated cantilever structure.

Overall, the masking process using Kapton tape demonstrates its effectiveness in defining the bottom contact region, but further refinements are necessary to enhance the masking accuracy and mitigate the shadowing effect. These findings provide valuable insights for future improvements in the fabrication process. Moreover, the results of the contact characterization and testing provide valuable insights into the conductivity and suitability of the aluminum and doped silicon contacts. The findings highlight the need for improved isolation between the contacts to eliminate leakage. These outcomes inform the development of alternative contact fabrication methods for successful beam contacting, which will be addressed in the future directions of this thesis.

4 Outlook

In the outlook of this thesis, it is evident that the contact fabrication method employed for the device was flawed, resulting in material overlap between the top and bottom contacts and consequently causing a leakage issue. This setback necessitates a thorough reevaluation of the entire contact fabrication procedure to ensure the successful realization of the device. Although the device could not be tested due to the inability to refabricate the contacts within the allotted timeframe, a proposed alternative method for contact fabrication will be presented. Additionally, an experimental design will be outlined, offering a promising avenue for future testing and evaluation of the device's performance.

4.1 Contact fabrication method

One of the primary challenges encountered in fabricating the contact lies in the magnetron sputtering process, which lacks the controlled direction of deposition present in e-beam evaporation. Unlike evaporation, sputtering involves material being sputtered in multiple directions, with atoms and molecules colliding from various angles. As a consequence, any unsealed openings in the structure become potential pathways for sputtered material, leading to undesirable overlap between the top and bottom contacts intended to be isolated.

To address this issue, two key problems need to be resolved within the available sputtering system. Firstly, the sample holder, where the sample is positioned upside down, must be modified. A new sample holder design is proposed, allowing the sample to be securely taped and ensuring its entire surface is exposed to the sputtered material. Secondly, a challenge arises from the inability to spin coat a resist layer without jeopardizing the integrity of the free-standing beams. To overcome this limitation, a heat-resistant tape is applied to protect the designated region.

To prevent material overlap and maintain a simple fabrication method, a dual-tape approach is adopted. As depicted in Figure 4.1a, the first layer of dielectric material is deposited after slightly shifting the tape farther back on the sample surface. Subsequently, in Figure 4.1c, the tape is reapplied, overlapping the newly deposited isolating layer. This ensures that any material deposited beneath the tape does not overlap with the bottom contact. The remaining layers are then deposited conventionally, as shown in Figure 4.1d.

By implementing this modified contact fabrication technique, the risk of material overlap can be effectively mitigated, contributing to the successful fabrication of the device.

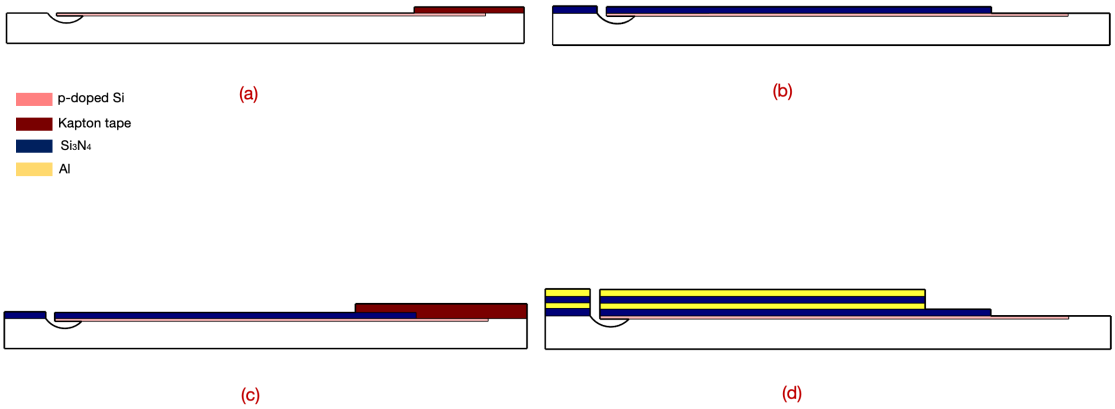

Figure 4.1: *Optimized nanofabrication process of the addition of the contact pads. a) Substrate is a silicon (100) wafer with a free-standing cantilever structure and elongated p-doped region for the contact pads strcuture. Using Kapton tape, the a part of the structure is masked to protect it from the next step. b) The masking tape is reapplied covering a part of the deposited structure, ensure electrical isolation. c) The stacked films are deposited on the entire sample, ending in a metallic Al top contact. d) The tape is removed to expose the bottom contact pad.*

4.2 Device testing

In order to study the properties of flexoelectricity, a method is needed to measure the strain caused by a voltage difference or the voltage difference generated by a strain. Given the challenges associated with miniaturizing mechanical bending appliances to the nanoscale, we have chosen to characterize this effect by measuring the bending caused by the polarization of our sample. This method involves applying an electric field to free-standing cantilevers and measuring the induced bending.

It is important to note that flexoelectricity μ can induce a curvature that is related to both a flexural rigidity of the plate D and the applied voltage V, as described by Equation 4.1.

$$k = \frac{\mu V}{D} \tag{4.1}$$

This flexural rigidity, which is a property of the cantilever, is given by Equation 4.2

$$D = \frac{Et^3}{12(1-\nu^2)}, \tag{4.2}$$

where E is Young's modulus, t is the thickness and ν is the Poisson ratio.

Additionally, the induced curvature of the beam scales as the cube of its thickness. Thus, the fabrication of planar capacitive cantilevers allows for the observation of this flexoelectric effect. [28]

4.2.1 Experimental setup

In order to perform these measurements, a system design for the observation of cantilever oscillations induced by an external alternating voltage is needed. The use of a laser beam interference method, as illustrated in Figure 4.2, is proposed.

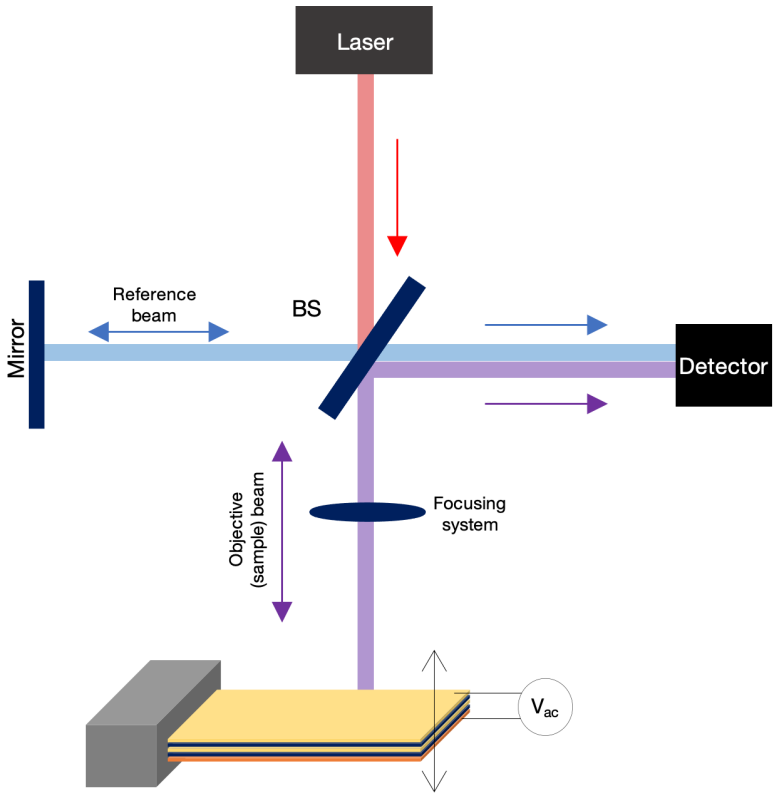

Figure 4.2: *Laser beam split at a 45-degree angle with a beamsplitter (BS), with half of the power focused on the oscillating cantilever and the other half directed towards a mirror. The reflection from both beams is then directed back to the beamsplitter, where it is combined and directed towards a detector.*

This method involves splitting a laser beam at a 45-degree angle, with half of the power focused on the oscillating cantilever and the other half directed towards a mirror. The reflection from both beams is then directed back to the beamsplitter, where it is combined and directed towards a detector. By using this technique, we can ensure that the distance traveled by the beam remains constant, allowing for the complete destructive

or constructive interference of the beams. As a result, oscillations in the cantilever can be accurately measured as fluctuations in power at the detector. This method is expected to provide high-precision measurements of the induced bending of the cantilever.

5 Summary and Conclusions

In this thesis report, the fabrication process of cantilever beams for the investigation of electromechanical coupling effects was described. The process involved several steps, including the fabrication of the cantilever structures and the addition of a Si_3N_4 layer. The results of each step were presented and discussed.

In the first step, the cantilever structures were fabricated using a combination of e-beam writing, selective etching, and spin-on-doping. The results showed that the beams underwent significant widening during the thermal drive-in process and subsequent etching. This widening was attributed to the permeation of boron under the oxide mask. It was also observed that only specific crystallographic orientations of the beams were successfully released and became free-standing, namely the <011> plane. Multiple tests of the etching process were conducted to achieve the desired etch stop effect.

In the second step, a Si_3N_4 layer was added to the cantilever beams to enhance their properties for flexoelectricity measurements. The Si_3N_4 layer was chosen for its wide bandgap, high dielectric constant, high thermal stability, chemical stability, and flexibility. The deposition process was optimized through several tests, and the best ratio of $Ar:N_2$ was determined to be 9:4. The resulting Si_3N_4 films exhibited low residual stress and aligned well with the ellipsometric model.

In conclusion, the fabrication process of the cantilever beams and the addition of the Si_3N_4 layer were successfully carried out. The results demonstrated the widening of the beams during the fabrication process and the importance of optimizing the etching process to achieve the desired etch stop effect. The Si_3N_4 layer addition showed promising results in terms of film quality and stress levels. These findings provide a solid foundation for further characterization and measurement of the flexoelectric properties of the fabricated cantilever beams.

The outlook of this thesis reveals the flawed contact fabrication method used for the device, resulting in material overlap between the top and bottom contacts and causing a leakage issue. To ensure the successful realization of the device, a thorough reevaluation of the contact fabrication procedure is necessary. Although the device couldn't be tested within the allotted timeframe due to the inability to refabricate the contacts, an alternative method for contact fabrication is proposed. Additionally, an experimental design is outlined to provide a promising avenue for future testing and evaluation of the

device's performance.

Regarding the contact fabrication method, the magnetron sputtering process employed lacks controlled deposition direction, leading to material overlap. Two key problems need to be addressed: modifying the sample holder design to expose the entire sample surface to the sputtered material and applying heat-resistant tape to protect the designated region during resist layer spin coating. To mitigate material overlap, a dual-tape approach is adopted, involving shifting and reapplied tape during the deposition process. This modified contact fabrication technique effectively reduces the risk of material overlap, ensuring successful device fabrication.

For device testing, the measurement of strain caused by a voltage difference or voltage difference generated by a strain is crucial to study flexoelectricity. In this case, the bending induced by the polarization of the sample is selected as the characterization method for the flexoelectric effect. The relationship between the induced curvature of the beam and flexural rigidity (D) and applied voltage (V) is described by the equation k = (μV) / D, where μ is the flexoelectricity, E is Young's modulus, t is the thickness, and ν is the Poisson ratio. By fabricating planar capacitive cantilevers, the flexoelectric effect can be observed.

To perform the measurements, an experimental setup utilizing a laser beam interference method is proposed. The method involves splitting a laser beam at a 45-degree angle, directing half of the power to the oscillating cantilever and the other half towards a mirror. The reflected beams are combined and directed to a detector, allowing for precise measurement of cantilever oscillations as fluctuations in power. This laser beam interference method is expected to provide high-precision measurements of the induced bending of the cantilever.

In conclusion, by addressing the contact fabrication flaws and adopting the modified contact fabrication technique, the successful realization of the device can be ensured. The proposed experimental setup using the laser beam interference method offers a promising avenue for future testing and evaluation of the device's performance in studying flexoelectricity.

References

[1] Mohammad Ibrahim Younis. “MEMS Linear and Nonlinear Statics and Dynamics”. In: 2011.

[2] Oliver Brand and Henry Baltes. “Micromachined Resonant Sensors — an Overview”. In: *Sensors Update* 4 (1998), pp. 3–51.

[3] Sandeep Kumar Vashist. “A Review of microcantilevers for sensing applications”. In: *AZojono - Journal of Nanotechnology Online* 3 (Jan. 2007), pp. 1–15.

[4] Wonjae Choi et al. “Energy Harvesting MEMS Device Based on Thin Film Piezoelectric Cantilevers”. In: *Journal of Electroceramics* 17 (Dec. 2006), pp. 543–548.

[5] Gustav Gautschi. “Piezoelectric Sensors”. In: *Piezoelectric Sensorics: Force Strain Pressure Acceleration and Acoustic Emission Sensors Materials and Amplifiers*. Berlin, Heidelberg: Springer Berlin Heidelberg, 2002, pp. 73–91.

[6] Mohsen Safaei, Henry Sodano, and Steven Anton. “A review of energy harvesting using piezoelectric materials: State-of-the-art a decade later (2008-2018)”. In: *Smart Materials and Structures* 28 (July 2019).

[7] Nipun Sinha et al. “Piezoelectric aluminum nitride nanoelectromechanical actuators”. In: *Applied Physics Letters* 95.5 (2009), p. 053106.

[8] Jürgen Rödel et al. “Perspective on the Development of Lead-free Piezoceramics”. In: *Journal of the American Ceramic Society* 92.6 (2009), pp. 1153–1177.

[9] V. Sundar and R. E. Newnham. “Electrostriction and polarization”. In: *Ferroelectrics* 135.1 (1992), pp. 431–446.

[10] Pavlo Zubko, Gustau Catalan, and Alexander K. Tagantsev. “Flexoelectric Effect in Solids”. In: *Annual Review of Materials Research* 43.1 (2013), pp. 387–421.

[11] David Codony. “Mathematical and computational modeling of flexoelectricity at mesoscopic and atomistic scales”. PhD thesis. UPC, Departament d’Enginyeria Civil i Ambiental, Mar. 2021.

[12] Thanh D. Nguyen et al. “Nanoscale Flexoelectricity”. In: *Advanced Materials* 25.7 (2013), pp. 946–974.

[13] H. Seidel et al. "Anisotropic Etching of Crystalline Silicon in Alkaline Solutions: I . Orientation Dependence and Behavior of Passivation Layers". In: *Journal of the Electrochemical Society* 137.11 (Nov. 1990), p. 3612.

[14] Peter J. Hesketh et al. "Surface Free Energy Model of Silicon Anisotropic Etching". In: *Journal of The Electrochemical Society* 140.4 (Apr. 1993), p. 1080.

[15] Helmut Seidel et al. "Anisotropic etching of crystalline silicon in alkaline solutions. II. Influence of dopants". In: *Journal of the Electrochemical Society* 137 (Nov. 1990), pp. 3626–3632.

[16] Alongkorn Pimpin and Werayut Srituravanich. "Review on Micro- and Nanolithography Techniques and Their Applications". In: *Engineering Journal* 16 (2012), pp. 37–56.

[17] Zhongping Wang and Zengming Zhang. "Electron Beam Evaporation Deposition". In: *Advanced Nano Deposition Methods*. John Wiley and Sons, Ltd, 2016. Chap. 2, pp. 33–58.

[18] Almas Bashir et al. "Chapter 3 - Interfaces and surfaces". In: *Chemistry of Nanomaterials*. Ed. by Tahir Iqbal Awan, Almas Bashir, and Aqsa Tehseen. Elsevier, 2020, pp. 51–87.

[19] K. Seshan and D. Schepis. "Sputter processing". In: *Handbook of Thin Film Deposition*. Elsevier, 2018, pp. 195–199.

[20] Rene Overney, George Tyndall, and Jane Frommer. "Springer Handbook of Nanotechnology". In: (Jan. 2004).

[21] Frank L. Riley. "Silicon Nitride and Related Materials". In: *Journal of the American Ceramic Society* 83.2 (2000), pp. 245–265.

[22] Michael Huff. "Review Paper: Residual Stresses in Deposited Thin-Film Material Layers for Micro- and Nano-Systems Manufacturing". In: *Micromachines* 13.12 (2022).

[23] G.C.A.M. Janssen et al. "Celebrating the 100th anniversary of the Stoney equation for film stress: Developments from polycrystalline steel strips to single crystal silicon wafers". In: *Thin Solid Films* 517.6 (2009), pp. 1858–1867.

[24] David Quirion et al. "Manufacturability and Stress Issues in 3D Silicon Detector Technology at IMB-CNM". In: *Micromachines* 11.12 (2020).

[25] H.Y. Liu et al. "Influence of sputtering parameters on structures and residual stress of AlN films deposited by DC reactive magnetron sputtering at room temperature". In: *Journal of Crystal Growth* 363 (Jan. 2013), pp. 80–85.

[26] D.L. Ma et al. "Optimal target sputtering mode for aluminum nitride thin film deposition by high power pulsed magnetron sputtering". In: *Vacuum* 160 (2019), pp. 410–417.

[27] Ryung Seol et al. "Flexoelectricity in barium strontium titanate thin film". In: (Jan. 2014).

[28] Umesh Bhaskar et al. "A flexoelectric microelectromechanical system on silicon". In: *Nature nanotechnology* 11 (Nov. 2015).